

Space- and Ground-Based Gamma-Ray Astrophysics

Stefan Funk ^{1, 2}

¹Erlangen Centre for Astroparticle Physics, Friedrich-Alexander-Universität
Erlangen-Nürnberg, Erwin-Rommel-Str. 1, D-91058 Erlangen, Germany

²Kavli Institute for Particle Astrophysics and Cosmology, Department of Physics
and SLAC National Accelerator Laboratory, Stanford University, Stanford, CA
94305, USA

Xxxx. Xxx. Xxx. Xxx. 2015. 00:1–47

This article's doi:
10.1146/((please add article doi))

Copyright © 2015 by Annual Reviews.
All rights reserved

Keywords

Dark Matter Cosmic rays Gamma-ray Astronomy Fermi-LAT Imaging
atmospheric Cherenkov Telescopes Galactic Center

Abstract

In recent years, observational γ -ray astronomy has seen a remarkable range of exciting new results in the high-energy and very-high energy regimes. Coupled with extensive theoretical and phenomenological studies of non-thermal processes in the Universe these observations have provided a deep insight into a number of fundamental problems of high energy astrophysics and astroparticle physics. Although the main motivations of γ -ray astronomy remain unchanged, recent observational results have contributed significantly towards our understanding of many related phenomena. This article aims to review the most important results in the young and rapidly developing field of γ -ray astrophysics.

1. INTRODUCTION

γ -ray astrophysics has seen a remarkable progress in recent years. High-energy observations of the Universe now represent a firmly established discipline in modern Astrophysics as they allow for studies of a broad range of topics related to the non-thermal Universe. The acceleration, propagation, and γ -ray radiation of relativistic particles is by now detected on a vast range of astronomical scales: from compact objects like neutron stars and solar mass black holes to cosmological scales such as other Galaxies and active galactic nuclei. At the same time, γ -ray astronomy can be considered as a discipline in its own right with interesting links to Cosmology and Particle Physics. Γ -ray photons travel in straight lines and therefore allow for an accurate determination of their origin. While γ rays often denote photons above 100 keV, (i.e. frequencies $\geq 10^{19}$ Hz), the focus of this review will be on astrophysical gamma rays above ~ 10 MeV (10^7 eV), the region where pair production into electron-positron pairs is the dominant interaction mechanism for photons. The highest-energy photons currently detected are in the range of 100 TeV (10^{14} eV) (1). Consequently, this review will cover an energy range of about 7 decades in energy. Recent results were obtained with both space-based instruments such as the *Fermi* Large Area Telescope (LAT) (2) and the AGILE satellite (3) and with ground-based observatories such as H.E.S.S. (4), MAGIC (5), and VERITAS (6). These observations have changed and deepened our understanding of energetic processes in the Universe and make this review timely.

Gamma rays are the highest-energy form of electromagnetic radiation. As such, the origins of gamma-ray astronomy are tightly connected to the scientific investigations into the origin of cosmic rays (CRs) – the highest energy particles in the Universe. First estimates for fluxes of cosmic gamma-ray sources (as a result of CR interactions) were given in a seminal paper by Morrison (7). These estimates turned out to be significantly overestimating the real fluxes, but they spawned a series of rocket and balloon experiments looking for gamma-ray emission from the sources of CRs. Space-based missions were used in those early days because Earth's atmosphere blocks gamma rays. Space-based observations in the early to mid-1960s mainly through satellites of gamma rays in the energy region around 100 MeV led to a number of breakthroughs in the study of the high-energy Universe. These came as first detection of gamma rays from space by Explorer XI (8) (mostly produced in interactions of CRs with the Earth atmosphere), with the first detection of gamma-ray bursts using the Vela satellites (9), and finally with the first detection of gamma rays from the interaction of CRs with interstellar material of the Milky way by OSO-3 (10). Subsequent years and decades saw significant improvement in the technology used in space-based detectors and orders of magnitude improvement were reached by employing instruments such as SAS-2 (11), COS-B (12), and EGRET (13).

During these times, also first ideas for observing gamma rays from the ground were developed. The ideas were based on the fact that in the interaction of gamma rays with the atmosphere the primary gamma ray gets lost, but secondary products are created that can be detected on the ground and that can be used to infer the properties of the astrophysical gamma rays. Already in the early 1950s (14) detected Cherenkov (optical) emission from atmospheric showers. The difficulty in the early days of this technique was how to suppress the much more numerous proton showers, that also generate Cherenkov light. Distinguishing gamma-ray induced showers from proton-induced showers based on their Cherenkov light turned out to be a significant challenge, although the basic idea to make use of the difference in shower development in the atmosphere (and thus in the image shape in the detector) was already suggested in the early 1960s (15). However, it took a

heroic effort mostly by groups in the US and in France to develop the technique to the point where the first astrophysical source (the Crab Nebula) could be detected at TeV gamma-ray energies from the ground (16). The main technical breakthrough was to use a pixelated camera to exploit the difference in shape of the atmospheric shower between gamma rays and protons and thereby suppress the background. The next big step forward came in the use of stereoscopy, i.e. by connecting several imaging Cherenkov telescopes to view the shower from different angles and further suppress the background (17). By now all major installations (H.E.S.S., MAGIC, VERITAS) employ a system of more than one telescope with pixelated cameras that cover a field of view of typically 5° diameter and $\sim 1000 - 2000$ pixels in each camera (18).

Our current view on the gamma-ray Universe is summarised in Figure 1, showing the gamma-ray sky above 1 GeV in Galactic coordinates as observed by the *Fermi-LAT*. As can be seen, the sky is composed of a broad band of diffuse emission along the Galactic plane, stemming from the interaction of the pool of Galactic CRs with interstellar gas and dust and in addition a collection of individual sources. The *Fermi-LAT* has provided significant new insights into the high-energy gamma-ray sky. Important discoveries include the observation of the pion-decay cutoff in the spectra of supernova remnants (SNRs), and multi-GeV components of gamma-ray bursts (GRBs), *etc* (see e.g. a review article by 19). The LAT also significantly enhanced our knowledge on the diffuse gamma-ray backgrounds. In particular, *Fermi-LAT* has extended the range of observations of the diffuse emission of the Galactic Disk and the isotropic (extragalactic) gamma-ray background to several hundreds of GeV. Since the energy spectrum of the Galactic diffuse emission is much softer (meaning that there are fewer high-energy photons) than many of the sources, the composition of the gamma-ray sky at higher (TeV) energies changes.

This review summarises the status of gamma-ray astronomy obtained through space-based and ground-based observations. It does not aim to provide a complete list of gamma-ray sources, nor does it aim for even a complete list of the different source classes. It aims to illustrate key science questions and describe their status by using selected observational results. The interested reader is referred to recent reviews covering related areas of research, such as a review of TeV astronomy (18), a review of pulsars at gamma-ray energies (20), a review of supernova remnants at high energies (21), reviews of dark matter observation with gamma rays (22, 23, 24, 25).

2. The Science Case for gamma-ray astrophysics

The suggestion that gamma rays traveling in straight line can reveal the sites of proton (and electron) acceleration in the Universe still constitutes the basis of one of the major objectives of the field. This concerns both the acceleration and propagation aspects of the study of CRs: while discrete gamma-ray sources indicate the sites of particle acceleration, the spatial distribution of the diffuse component of radiation provides information about the propagation of relativistic particles in the ambient magnetic fields. Gamma rays are produced in the interaction of accelerated *charged* particles (nuclei or electrons or positrons) with interstellar (target) material or magnetic or radiation fields. Once these *targets* for the radiation, i.e. the gas densities (pion-decay and Bremsstrahlung), magnetic (synchrotron emission) or radiation fields (inverse Compton scattering) are known through multi-waveband studies the detection of gamma rays allows for a determination of the detailed spatial and energy distribution of high-energy charged particles in our Universe. While the exploitation of this

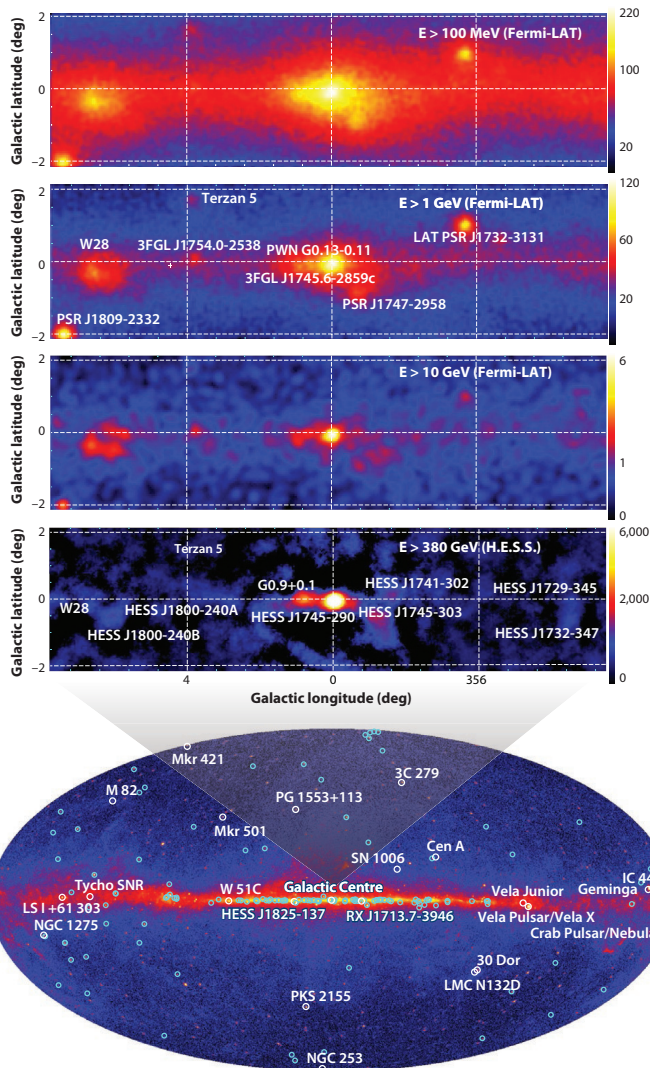


Figure 1

(Bottom) The high-energy γ -ray sky. The colors correspond to intensity per pixel (i.e., counts divided by exposure and solid angle) for Pass 8 Source class (PSF 3 event class), for γ -rays above 1 GeV. The positions of discrete TeV γ -ray sources detected with ground-based instruments are marked by cyan circles or white circles taken from TeVCat (<http://tevcad.uchicago.edu>). (Top) Zoomed-in view into the Galactic center region ($|l| < 8^\circ$, $|b| < 2^\circ$; corresponds to a size of $1,100 \times 280$ pc) for different minimum energies. Several prominent sources from the 3FGL catalog are marked in the second panel. Note that a significant number of sources from 3FGL are not marked. The fourth panel shows a H.E.S.S. excess map from the Galactic plane survey as published for 2004 data (24) above 380 GeV. The TeV-detected sources from TeVCat are marked, although certain areas of this region received a significantly larger number of observations in subsequent years.

The Key Science Questions

Photon radiation in the gamma-ray band differs fundamentally from lower energy radiation: MeV to TeV gamma rays cannot be created thermally in celestial systems. Instead, more exotic processes allow the concentration of large amounts of energy into a single quantum of radiation. The key science question can be broadly classified into four main areas:

The origin of Cosmic rays

The acceleration of particles to the highest energies in astrophysical objects is of fundamental importance for high-energy astrophysics. Main questions that can be addressed by MeV to PeV gamma-ray observations are: a) which sources provide the bulk of the Galactic CRs, b) what is the spectrum of the accelerated particles and c) what is the particle acceleration mechanism responsible for CRs?

Dark matter annihilations

The observation of gamma rays from the Universe provides a chance of observing indirect (self-annihilation) signatures of DM. Numerous and diverse hints point to the existence of weakly interacting massive particles (WIMPs) with masses in the range $\sim 0.01 - 10$ TeV as the most plausible form of DM. If true, gamma-ray observations offer a compelling way to connect signals found in the Large Hadron Collider at CERN or in direct detection experiments to the actual distribution of DM in the Universe. Gamma rays also allow for the detection of signatures of axions via the distortion of energy spectra of distant sources through axion-photon mixing in intervening magnetic fields.

Relativistic Outflows

Particle acceleration occurs in relativistic outflows such as winds or jets. These collimated streams of relativistic plasma are commonly seen in many prominent gamma-ray source classes, such as active galactic nuclei, gamma-ray bursts, and in Galactic binary sources. The accretion of material onto black holes and other very compact objects often leads to the formation of a collimated jet of plasma that travels outward along the axis of the accretion disk. The formation, internal structure, and evolution of collimated jets are still not fully understood. Gamma-ray observations can help to reveal the most energetic of these relativistic outflows and can add to our understanding of the processes governing these enigmatic objects.

Cosmological questions

Active Galactic nuclei (AGN) comprise the largest number of gamma-ray sources detected by now. Given the large distances between us and many of those extragalactic gamma-ray emitters, they can be used to study properties of the intervening space. As such, gamma rays can be used to put constraints on intergalactic magnetic and photon radiation fields in the Universe. Additionally, gamma rays can be used to probe voids in the Universe and test fundamental properties of quantum gravity.

This review focusses on the origin of cosmic rays and the search for dark matter annihilation. For the other two topics the reader is referred to reviews such as (26, 27).

potential remains one of the highest priority motivations of the field, the observational and theoretical studies of recent years revealed new exciting aspects. Most importantly, the physics and astrophysics of relativistic outflows such as pulsar winds and active galactic nuclei (AGN) jets and the exciting issues related to the cosmological probes of the extragalactic radiation and magnetic fields using the beams of gamma rays emitted by objects located at large redshifts. In addition, the study of cosmic gamma rays promises interesting potential related to the indirect search for Dark Matter (e.g. 28) and the exploration of possible deviations in fundamental rules of physics like violation of the Lorentz invariance (e.g. 29).

2.1. Particle Acceleration in astrophysical objects

A long-standing mystery is the mechanism by which CRs (protons, electrons and positrons as well as higher nuclei) are accelerated in our galaxy. The main properties of CRs can be derived from the locally detected spectrum of these particles. They consist mostly of protons with smaller fractions of higher nuclei and electrons. The all-particle spectrum of CRs can be described by a power-law in energy $dN/dE \sim E^{-\Gamma}$ with an index of $\Gamma = 2.7$ below the *knee* at $\sim 10^{15}$ eV (1 PeV) above which the index changes to $\Gamma \sim 3.1$ continuing to about 10^{19} eV. It is generally assumed that the Galactic CRs below the knee are produced by a single mechanism (and probably single source class), whereas both galactic and extragalactic sources have been suggested above the knee. The remnants of supernova explosions could sustain the flux of CRs if they were to put $\sim 10\%$ of their bulk (explosion energy) into the acceleration of CRs. Whatever the sources of CRs are: to populate the Galactic CR pool each source must on average provide of order 10^{48} ergs year $^{-1}$ in protons with a power law in energy and a spectral index of ~ 2.2 up to energies of $\sim 10^{15}$ (at least for part of their lifetime). Also the acceleration of electrons is an important topic. Beyond the study of shock accelerating objects, relativistic outflows, such as collimated jets from black holes and other compact objects are important test cases for particle acceleration in the universe

2.2. Dark Matter Annihilation

In the standard cosmological model, dark matter (DM) dominates the mass density in the Universe and is the driving force in structure formation. A favoured candidate for dark matter particles are weakly interacting massive particles (WIMPs)(see e.g. 30, 31), initially in equilibrium in the early Universe, but then frozen out due to the rapid expansion of the Universe. The observed DM density arises naturally if masses of DM particle in the GeV to TeV range are assumed, and annihilation cross sections are on the weak interaction scale. DM candidates include the lightest and stable supersymmetric particle (32), or Kaluza-Klein particles predicted in theories with extra dimensions (for a review see e.g. 33). DM particles are cold – i.e. non-relativistic – and they accumulate at the centers of galaxies, but also in substructures in the halos of galaxies. WIMP dark matter particles are expected to mutually annihilate, giving rise to the creation of particles and of gamma rays with energies up to the mass of the dark matter particles (assuming the velocities are so small that annihilation is effectively almost at rest).

The search for signs of dark matter particles is a key topic in high energy astrophysics(see 34, 35, for reviews and references) and especially in high energy gamma-ray astronomy. Even if dark matter candidates such as supersymmetric WIMPs were produced in accelerators on Earth, it will be difficult to prove that these particles are stable over the lifetime of the

Universe, and can account for astrophysical dark matter; an astrophysical detection will be required.

2.3. Other Cosmological probes

A violation of Lorentz invariance may manifest itself as a modification of the energy-momentum relation of photons, as predicted in some models of quantum gravity due to the modified structure of space-time on the Planck scale (see 36). Corrections to the energy-momentum relation are therefore generally predicted to scale as some power of E/M_{Planck} , with $M_{\text{Planck}} = 1.22 \times 10^{19}$ GeV. Effects can manifest themselves either as a energy dependence of the speed of propagation, or by allowing certain reaction channels which normally would be kinematically forbidden.

To search for energy-dependent variations of the speed of light, one needs (a) a source emitting gamma rays at a well-defined moment and a precise measurement of arrival times, with a combined precision Δt , (b) a wide energy coverage of gamma rays ΔE and (c) a long propagation path D . Limits obtained using TeV gamma rays from AGN approach the Planck scale (37, 38), and limits for GeV gamma rays exceed the Planck scale (39).

The light emitted by stars and accreting compact objects through the history of the Universe is encoded in the intensity of the extragalactic background light (EBL). Knowledge of the EBL is therefore crucial to determining the nature of star formation and galaxy evolution. After the cosmic microwave background, the EBL produces the second-most energetic diffuse background. Understanding of the EBL is thus also essential for understanding the full energy balance of the Universe. Generally, direct measurements of the EBL are limited by Galactic and other foreground emissions. However, the imprint of the EBL on gamma rays propagating cosmological distances can be measured (40). A gamma-ray photon of energy E_γ and an EBL photon of energy E_{EBL} can annihilate into an electron-positron pair. This process becomes most effective for collisions when $E_\gamma \times E_{\text{EBL}} \leq 2(m_e c^2)^2$, where $m_e c^2$ is the rest mass energy of the electron. This process attenuates the spectra of gamma-ray sources above a critical gamma-ray energy of $E_{\text{crit}}(z) \approx 170(1+z) - 2.38$ GeV (41). All current results indicate a rather low level of EBL in the universe, thereby placing strong constraints on the existence of an unseen population of stars in the early Universe or indicating that gamma-ray photons converting to axions and back to gamma rays in strong magnetic fields on the way from the source to us, thereby being unavailable to the process of photon-photon pair productions for parts of the journey (42, 43).

3. Gamma-ray production

3.1. Leptonic emission

For the gamma-ray spectra one typically starts with an accelerated power-law spectrum of the charged particles (potentially with a high-energy cutoff at E_{max} as discussed in section 2.1) and subsequently calculates the losses into photons from the different processes. Each of the different processes has certain characteristic features that can be used to identify the underlying production mechanism once the gamma rays are observed.

The spectral shape of the synchrotron spectrum is strongly peaked with a tail to higher energies. For an isotropic distribution of pitch angles, a population of mono-energetic

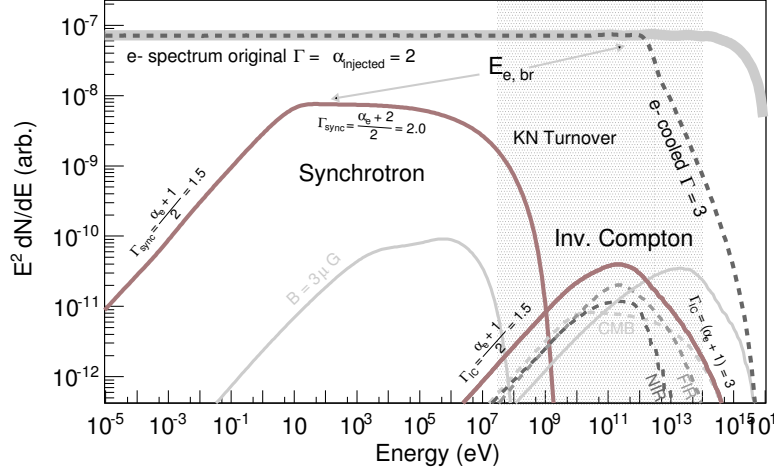


Figure 2

Spectral energy distribution of electrons at injection (light gray with $\alpha_{\text{injection}} = 2.0$) and the steady state including cooling (dashed dark gray) for a source with age $t_{\text{age}} = 1000$ yrs, $B = 100\mu\text{G}$, for a scenario in the inner 100 pc of our Galaxy. The cooling break in the electron spectrum at ~ 1.2 TeV is apparent in the steady-state electron distribution (dashed dark gray), in the synchrotron spectrum and in the IC spectrum. Also apparent is the turnover in the spectra at even higher energies due to KN cooling which incur catastrophic losses on the electrons. The case for a much lower B-Field of $3\mu\text{G}$ is also shown in light gray. The shaded gray region shows the sensitive range of current gamma-ray detectors (*Fermi*-LAT, IACTs).

electrons with energy E_e will emit synchrotron photons at an energy E_{sync} with (44):

$$E_{\text{sync}} = 0.2 \frac{B}{10\mu\text{G}} \left(\frac{E_e}{1\text{TeV}} \right)^2 \text{ eV} \quad (1)$$

The synchrotron radiation spectrum of TeV electrons in a typical $10\mu\text{G}$ magnetic field thus peaks at approximately 0.2 eV (i.e. in the visible range of the electromagnetic spectrum). A more realistic case is one where the electron population has a distribution of energies that follows a power-law with index α_e (45). The differential synchrotron spectrum in this case follows a power-law with index $\Gamma_{\text{sync}} = (\alpha_e + 1)/2$. Energy losses in the IC Thomson regime and for synchrotron emission are proportional to E_e^{-1} . These losses will therefore modify the initial power-law distribution of electrons so that the steady state energy spectrum of the electrons will have a break from α_{injected} to $\alpha_{\text{injected}} + 1$ (see Figure 2). The break will be at an energy where the cooling time scales become comparable to the age t_{age} of the source (44) and can be approximated as $E_{e,\text{br}} = 1.2 \times 10^4 (B/10\mu\text{G})^{-2} (t_{\text{age}}/10^4\text{yr})^{-1}$ GeV. This break will induce a corresponding break in the synchrotron and IC spectrum by $\Delta\Gamma = 0.5$ at an energy that can be determined by inserting $E_{e,\text{br}}$ into equation 1.

For electrons, the inverse Compton scattering of mono-energetic electrons on a population of target photons (e.g. a black-body spectrum) produces a broad spectral distribution of high-energy photons. This distribution peaks at

$$E_{\text{IC}} = 5 \times 10^9 \frac{E_{ph}}{10^{-3}\text{eV}} \frac{E_e}{1\text{TeV}}^2 \text{ eV} \quad (2)$$

Due to the similarity of equations 1 and 2 the spectra for synchrotron emission and for IC scattering have the same shape (albeit at different energies). Like in the case of synchrotron emission, for a continuous injection of electrons with a power-law distribution of the form $dN/dE \propto E_e^{-\alpha}$ the inverse Compton spectrum in the Thomson regime will have a slope of $\Gamma = (\alpha + 1)/2$. In the KN regime the IC spectrum will be significantly steeper $\Gamma = (\alpha + 1)$. Therefore, even a power-law distribution of electrons will produce a break in the spectrum of the gamma-ray emission due to the onset of the KN regime.

3.2. Hadronic emission

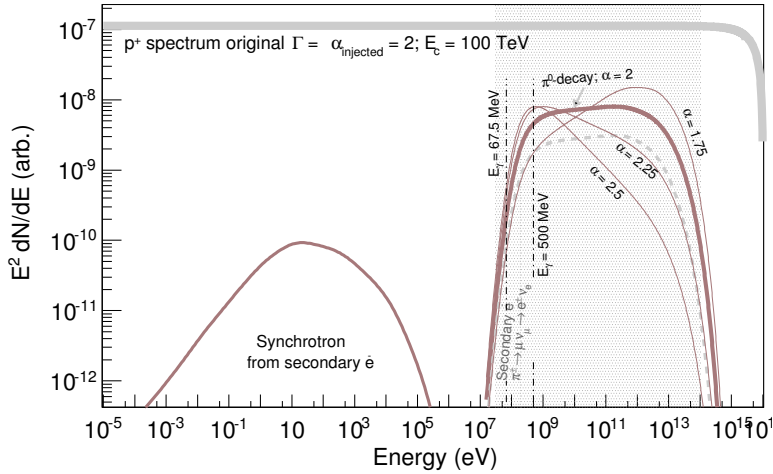


Figure 3

Spectral energy distribution of accelerated protons (powerlaw index $\alpha_{\text{injection}} = 2.0$ and cutoff at 100 TeV) and gamma rays resulting from inelastic collisions with interstellar material. The dominant emission into photons is via the decay $\pi^0 \rightarrow \gamma\gamma$ (solid brown). As can be seen, the gamma-ray spectrum follows the parent protons spectrum rather closely in the mid-energy range and the high-energy cutoff region. For all proton indices the low-energy turnover is a characteristic feature of the pion-decay emission. Also shown is the spectrum of electrons resulting from the inelastic pp-interactions via the decay chain $\pi^\pm \rightarrow \mu + \nu_\mu \rightarrow e^\pm \nu_e$ (dashed gray). For the synchrotron emission from these so-called secondary electrons a source with age $t_{\text{age}} = 1000$ yrs, and $B = 30\mu\text{G}$ has been assumed. The shaded gray region shows the sensitive range of current gamma-ray detectors (*Fermi*-LAT, IACTs).

Figure 3 shows the gamma-ray spectral energy distribution (SED) for a proton spectrum with $\alpha = 2$, $E_c = 100\text{TeV}$. Cooling plays a relatively minor role in sources actively accelerating particles, since even in the case of a typical Galactic density $n = 1\text{cm}^{-3}$ the cooling time is of the order of 10^7 years. The shape of the gamma-ray energy spectrum away from the threshold directly mirrors the shape of the parent proton spectrum. The total fraction of the energy of each incident proton converted into gamma rays is approximately $\kappa = 0.17$. It has been shown (see e.g. 46) that for proton spectrum indices of 2.1 – 2.7 the emissivity, i.e. the number of gamma rays produced per H-atom in the interaction of accelerated protons with interstellar material is $q_\gamma(> 100\text{MeV}) \approx 0.5 \times 10^{-13} \text{s}^{-1} \text{erg}^{-1} \text{cm}^3 (\text{H} - \text{atom})^{-1}$. This can be turned into a flux at Earth by an astrophysical accelerator putting a fraction

ϵ_{CR} of its energy output E_{pr} into acceleration of protons:

$$F_{\gamma}(> 100\text{MeV}) = 4.4 \times 10^{-7} \epsilon_{\text{CR}} \frac{E_{\text{pr}}}{10^{51}\text{erg}} \frac{d}{1\text{kpc}}^{-2} \frac{n}{1\text{cm}^{-3}} \text{cm}^{-2} \text{s}^{-1} \quad (3)$$

I.e. if distance d and density of the interaction region n is known, the amount of energy in protons E_{pr} at the interaction site can be directly inferred from the gamma-ray flux F_{γ} . It should be noted, that for an energy-dependent diffusion coefficient high-energy particles might propagate ahead of lower-energy particles. Dense regions ahead of the shock would therefore not be fully permeated by the particles and therefore “see” particles with an effective low-energy cutoff. Particles with different energies would therefore encounter different gas density and the resulting gamma-ray spectrum will no more follow the proton spectrum (see e.g. 47, for a comprehensive discussion).

Given the similarity of the gamma-ray spectra emitted by accelerated electrons and those emitted by accelerated protons, the low-energy part becomes a crucial tool in distinguishing the different scenarios. For kinematic reasons, the decay of $\pi^0 \rightarrow \gamma\gamma$ imparts each gamma ray with an energy $E_{\gamma} = m_{\pi^0}c^2/2 = 67.5$ MeV in the rest frame of the neutral pion. The resulting gamma-ray number spectrum dN_{γ}/dE_{γ} , is thus symmetric about 67.5 MeV in a log-log representation (48). The π^0 -decay spectrum in the usual $E_{\gamma}^2 dN_{\gamma}/dE_{\gamma}$ representation rises steeply up to ~ 400 MeV (the exact turnover in this representation depends on the parent proton spectrum as shown in Figure 3). This characteristic spectral feature (often referred to as the “pion-decay bump”) uniquely identifies π^0 -decay gamma rays and thereby high-energy protons, allowing a measurement of the source spectrum of CRs.

Electron bremsstrahlung and pp inelastic scattering both depend on the density of ambient medium n_0 . Assuming that electrons and protons are accelerated with the same power-law spectrum, the ratio of gamma-ray emissivities (i.e. the emission rate per hydrogen atom) can be estimated as $q_{\gamma}^{\text{br}}/q_{\gamma}^{\pi^0} \sim R3\tau_{pp}/\tau_{Br} = 4R$ where R is the electron to proton ratio. For typical values of $R \leq 10$ as in the expected sources of Galactic CRs pion production at high energies dominates over bremsstrahlung gamma rays.

3.3. Dark Matter Decay or Annihilation

The flux of gamma rays from annihilation processes is given by a product of a factor depending on particle physics properties of DM particles, and a factor depending on their astrophysical distribution (49)

$$\phi = \left(\frac{\langle \sigma v \rangle}{M^2} \frac{dN_{\gamma}}{dE} \right) \left(\frac{1}{4\pi} \int_{\text{LOS}} \rho^2 dl \right) \quad (4)$$

where $\langle \sigma v \rangle$ is the velocity-weighted annihilation cross section of DM particles of mass M , dN_{γ}/dE the gamma-ray spectrum per annihilation event, and the second factor is the line-of-sight integral of the squared DM particle density ρ^2 . The gamma-ray emission from DM annihilation can often be described as a combination of several processes and depends strongly on the annihilation channel (see Figure 4). The most common of these contribution is usually the hadronisation of decay or unstable particles. Supersymmetric models typically predict the annihilation of the lightest supersymmetric particle (often the neutralino) into heavy final states consisting of $b\bar{b}$, $t\bar{t}$ or $\tau^+\tau^-$ or ZZ , W^+W^- etc. Each of these channels (with the exception of annihilation into $\tau^+\tau^-$) produce very similar (*continuum*) spectra of gamma rays, ultimately dominated by the decay of (secondary) mesons such as

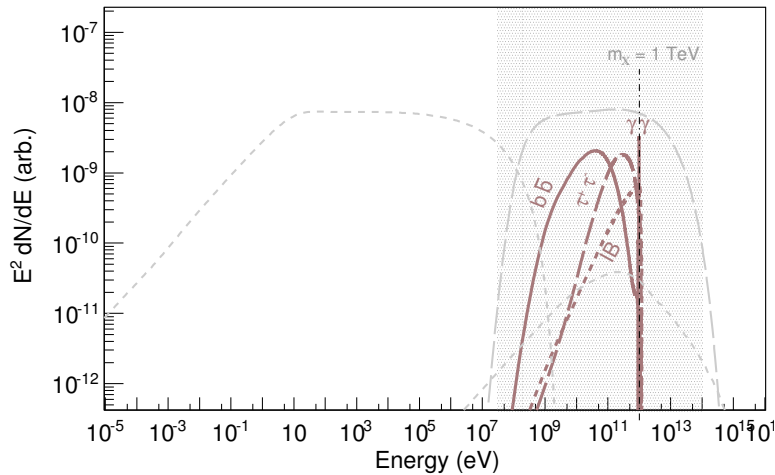


Figure 4

Spectral energy distribution of gamma rays resulting from neutralino annihilation (solid brown) with mass $m_\chi = 1$ TeV. The spectrum consists of 4 (main) components: continuum emission from quarks and bosons (labeled $b\bar{b}$ shown here as an example), continuum emission from heavy leptons (labeled $\tau^+\tau^-$), internal bremsstrahlung from annihilation into leptons (e^+e^- and $\mu^+\mu^-$ labeled IB) and line emission into $\gamma\gamma$ and $Z\gamma$ etc). The relative strength of these components depends on the particle physics model chosen for the annihilation. The typical astrophysical foreground spectra from accelerated electrons and accelerated protons are also shown in light gray (see Figures 3 and 2) for comparison. The shaded gray region shows the sensitive range of current gamma-ray detectors (*Fermi*-LAT, IACTs).

π^0 and therefore resembling the broad spectra seen in the more traditional (IC or π^0 decay) channels discussed above with a cutoff at the dark matter mass (see Figure 4 labeled $b\bar{b}$). The spectra are softer for annihilation into b quark pairs, compared to light quark pairs. Annihilation may also proceed directly into the two-gamma (or the γZ) channel, via a loop-level process, resulting in gamma-ray lines (28) as perfect signature, but the cross sections are in most models strongly suppressed. If helicity arguments disfavor annihilation into two fermions, as is the case in certain classes of models, radiative corrections (so-called internal Bremsstrahlung 50) may enhance annihilation channels where the gamma-ray spectrum mimics a broad line near the kinematic limit (see Figure 4 labeled IB). For a more detailed review see e.g.(22, 23).

4. Status of instrumentation

Gamma rays span an energy range of about 7 decades in energy and subsequently a typical flux difference of 14 decades between the low and the high-energy end. Consequently, not one technique or instrument can cover the whole energy range. While at the low energy end a bright source such as e.g. the Vela pulsar exhibit $\approx 10^{-1}$ photons $\text{m}^{-2} \text{s}^{-1}$ (or the Crab Nebula $\approx 10^{-3}$ photons $\text{m}^{-2} \text{s}^{-1}$) above 100 MeV, at the high energy end the brightest source such as the Crab Nebula exhibit $\approx 10^{-7}$ photons $\text{m}^{-2} \text{s}^{-1}$. While one usually wants to build instruments with detection areas as large as possible, at low energies $\mathcal{O}(1\text{m})$ are

appropriate, while at high-energies areas ($> 50 \text{ GeV}$) $\mathcal{O}(10^4 m)$ are needed.

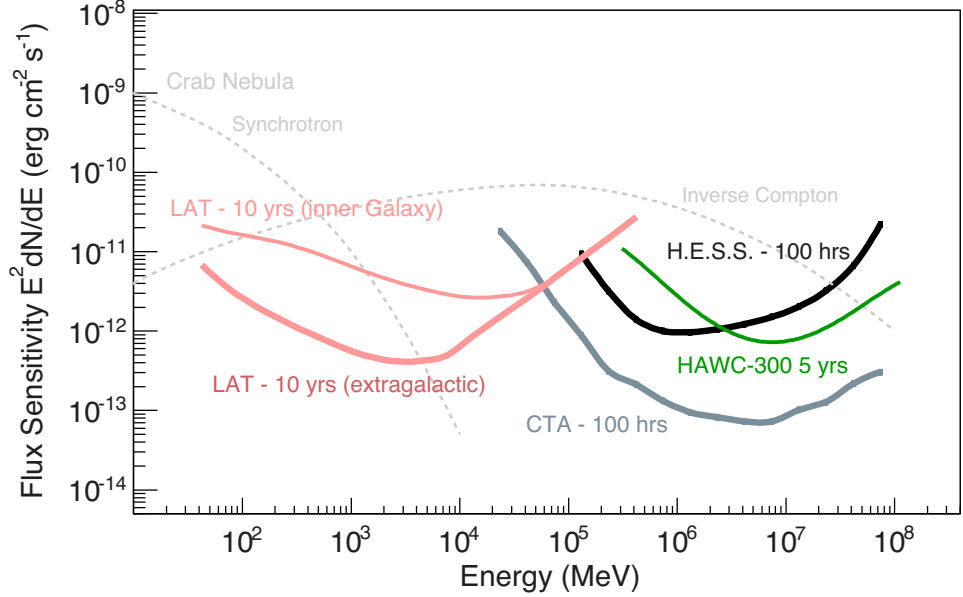


Figure 5

“Differential” sensitivity (integral sensitivity for 4 bins of energy per decade) for a minimum significance of 5σ in each bin, minimum 10 events per bin. For *Fermi*-LAT, the curve labeled “inner Galaxy” corresponds to the background estimated at a position of $l = 10^\circ, b = 0^\circ$, while the curve labeled “extragalactic” is calculated for $l = 10^\circ, b = 90^\circ$. For the ground-based instruments a 5% systematic error on the background estimate has been assumed. For the *Fermi*-LAT, *Pass8SourceV5* instrument response function curves have been used (number of events $n = 10$ and $TS = 25$ per bin). For comparison, the synchrotron and Inverse Compton measurements for the brightest persistent TeV source, the Crab Nebula are shown as dashed grey curves. The HAWC sensitivity (in green) was reproduced from (51).

However, the atmosphere blocks gamma rays from reaching the ground. Therefore their direct detection needs space-based instruments. At higher energies the detection area of space-based detectors is insufficient, so that a ground-based technique is needed. Ground-based instruments operate on the principle of detecting the secondary products of the interaction of gamma rays with the atmosphere. In this interaction a particle shower in the atmosphere gets created consisting mostly of electrons and positrons (in the case of a gamma-ray or electron-initiated showers) or of electrons and muons (in the case of proton-initiated showers). The two main techniques that utilize the air shower techniques are *Imaging Atmospheric Cherenkov Telescopes (IACTs)* that detect the (optical) Cherenkov light produced by the shower particles in the atmosphere and *Water Cherenkov Detectors* that directly detect the particles through the Cherenkov light produced in water detectors on the ground. Since the latter require the particles to reach the ground, their threshold is usually higher ($\sim 100 \text{ GeV}$), but they can operate continuously while the IACTs can only operate during dark night time (to be able to detect the faint Cherenkov light from the shower).

All detection techniques must deal with the common issue that in order to detect a significant signal of gamma rays the much more numerous background of CR protons has to be suppressed. This is usually done by an active veto for charged particles (in the case of space-based detectors) or by making use of the difference in shower development (mostly shower shape and muon content) between a gamma-ray induced electromagnetic shower and a proton-induced hadronic shower. Typical suppression factors are $\sim 10^{-6}$ for the *Fermi*-LAT, up to $\sim 10^{-5}$ for IACTs (with an angular cut optimised for point-sources) and several 10^{-3} for Water Cherenkov detectors such as HAWC (51).

The detection techniques are complementary in various aspects as illustrated in Figure 5: while the space-based detectors are ideally suited for the low-energy part of the spectrum starting at ~ 30 MeV even the largest operating instruments such as the *Fermi*-LAT typically run out of sufficient detection area at around ~ 100 GeV (for the brighter sources). This is the regime that corresponds to the threshold energy of the IACTs where enough Cherenkov light in the particle shower in the atmosphere gets produced to trigger a typical ~ 10 m mirror diameter IACT. At the highest energies (~ 30 TeV for the brighter sources) the IACT again run out of detection area and this is the regime where covering the ground with a large number of water Cherenkov telescopes can provide the necessary detection areas. A detailed comparison of the sensitivities of space-based and future ground-based instruments reveals that IACTs will be more sensitive than the *Fermi*-LAT for measuring spectra of sources with an E^{-2} spectrum above ~ 40 GeV (52).

Given all these different observational efforts the current time can be seen as “Golden age” for gamma-ray astronomy with a variety of currently operating instruments that if used in conjunction offer observations over more than 7 decades in energy with high angular resolution (typically up to $\sim 0.1^\circ$) and significant coverage of the sky at any given moment.

4.1. Space-based observatories

Space-based detectors above 20 MeV operate on the principle of pair-creation in the detector. The main instrument in this energy range is the *Fermi Gamma-ray Space Telescope* (FGST, formerly GLAST) launched in June 2008. The *Fermi* LAT (Large Area Telescope) yields observations in the energy range between ~ 20 MeV and ~ 300 GeV. The instrument consists of a *tracker* to measure the tracks of the electron-positron pair created in the pair-creation of the gamma ray, a *calorimeter* to determine the energy of this electron-positron pair (and hence of the primary gamma ray) and an *anti-coincidence detector* to veto the charged particle background. The tracking section of the LAT has 36 layers of silicon strip detectors interleaved with 16 layers of tungsten foil to facilitate the pair-creation (12 thin layers, 0.03 radiation length, at the top followed by 4 thick layers, 0.18 radiation length, in the back section, adding up to a total radiation length of $\sim 1X_0$). The total surface area of the LAT is $\approx 1.8\text{m} \times 1.8\text{m}$ with about 80% of that being sensitive tracker area. The calorimeter is composed of an 8-layer array of CsI crystals (8.5 total radiation lengths). The segmented anti-coincidence detector surrounding the tracker consists of plastic scintillators read out by photomultiplier tubes. The instrument typically triggers at a rate of $\sim 3\text{kHz}$, completely dominated by the proton background. About 90% of the events are discarded on the fly resulting in a down-link rate of about 450 Hz (90% of these are events that pass the gamma-ray filter, with an additional 25 Hz of diagnostic filter and 5 Hz of a Heavy ion filter). On the ground, these events are reconstructed and additional gamma-hadron separation cuts applied. The total photon rate after background rejection cuts is a few Hz.

The effective collection area of the LAT (taking into account gamma rays that are lost during the removal of the charge particle background) is about 0.65m^2 above $\sim 1\text{GeV}$. For this energy range, the *Fermi*-LAT provides an unprecedented angular resolution (0.8° at 1 GeV averaged over the LAT acceptance and better than 0.2° at energies above 10 GeV). It is a well designed tool for deep surveys of the gamma-ray sky with a large field of view of 2.4 steradian (at 1 GeV) (53). The live time of the instrument is $\approx 75\%$ – the main factors limiting this fraction being the South Atlantic Anomaly (54) when the instrument is switched off (13%) and the readout dead-time fraction (9%). More information about the design of the LAT is provided in (2), the in-flight calibration of the LAT is described in (53). One advantage over ground-based detectors is that the instruments can be calibrated in the laboratory (since the atmosphere is not part of the detector). *Fermi*-LAT has been tested in various beam tests (55) before launch. The resulting systematic error in the effective area of the *Fermi*LAT has been estimated to be 10% below 100 MeV, 5% at 562 MeV, and 20% above 10 GeV with linear interpolation in logarithm of energy between the values (56).

Over the last 7 years, *Fermi* LAT has provided a significant improvement in our understanding of the MeV to GeV gamma-ray sky (see e.g. Fig.1). The results confirm the (optimistic) pre-launch expectations that included a dramatic increase of the number of gamma-ray emitting pulsars and AGN (more than 1200 by now), discovery of new classes of *compact/variable* and *extended* galactic and extragalactic gamma-ray sources,

Important results have also been contributed by the Italian gamma-ray satellite AGILE (Astrorivelatore Gamma ad Immagini LEggero - Light Imager for Gamma-ray Astrophysics)(3). AGILE's main instruments, the gamma-ray imager (GRID) is similar to *Fermi*-LAT but on a smaller scale. It consists of a Tungsten-Silicon tracker and of a CsI calorimeter. The tracker consists of 14 planes of area $\sim 40\text{cm} \times 40\text{cm}$ (i.e. significantly smaller surface area than the LAT) with a total radiation length of $1X_0$ (like in the case of the LAT). The on-axis effective area is about 0.04 m^2 (compare to $\sim 0.8\text{m}^2$ for the LAT).

4.2. Ground-based observatories

Ground-based observatories have in common that they detect the secondary products of the interaction between the gamma ray and the atmosphere (the shower particles). While IACT detect the Cherenkov light of the shower particles in the atmosphere, Water Cherenkov detectors detect the Cherenkov light of the shower particles in the detector (the water tanks). These detectors typically have three operating regimes: at the low energy end (the threshold region) the sensitivity is governed by the ability to trigger the detector and the relevant question is whether the energy of the gamma ray is large enough to produce enough Cherenkov light in the atmosphere (or energetic enough showers to reach the ground) to trigger the detector. The thickness of the atmosphere at ground-level is $\sim 1000\text{gcm}^{-2}$ which corresponds to about 1 m of lead or ~ 28 radiation lengths. The shower typically starts with pair-creation of the gamma ray into an electron positron pair at an altitude of $\sim 20\text{km}$ above ground. The depth of the shower maximum X_{max} depends logarithmically on the energy of the gamma ray. For a 1 TeV gamma rays, X_{max} corresponds to an altitude of 10 km above sea level. The background of charged particles (mostly protons) also producing air showers is up to 10^4 larger than rate of gamma rays. To efficiently suppress this background the shape and composition of the air shower in the atmosphere as well as the expected direction from which the gamma rays are arriving are the main handles.

4.2.1. Imaging Atmospheric Cherenkov Telescopes. In recent years these instruments have emerged as the most sensitive detectors for observing gamma rays above ~ 50 GeV. They map the Cherenkov light of the air showers with mirrors onto a fast camera in the focal plane of the mirrors and thereby measure the angular distribution of the Cherenkov light from the air shower. Gamma-ray induced showers have typical rms widths and rms length of 0.1° and 0.3° . A pixelation in the camera much finer than this rms width does not seem to be very effective.

A few basic instrument requirements can be derived from the aforementioned 1 TeV shower: the (mainly blue) Cherenkov light arrives in a ring on the ground with a radius of ~ 120 m at an altitude of 2000 m. Stereoscopic observations have been demonstrated to be important for background rejection (significantly suppress hadronic showers in which long-lived muons can trigger individual telescopes at the trigger level) and for angular resolution. The spacing of the telescopes should thus be ~ 100 m. Closer spacing allows for an improvement of the low-energy performance at the expense of collection area at higher energies (and vice versa). The total amount of light is proportional to the total track length of all the particles in the shower – which in turn is proportional to the energy of the primary particle – and thus provides a calorimetric measurement of the shower. Typically, ~ 100 photons m^{-2} per TeV of primary energy reach the ground at 2000 m altitude; at sea level this number drops to $\sim 10m^{-2}$. For typical efficiencies of IACTs to detect photons ($\sim 10\%$ – mirror losses, quantum efficiency of detectors) $\sim 100m^2$ of mirror area are needed to trigger a telescope with 100 photo-electrons for a 0.1 TeV shower. The thickness of the light front is ~ 1 m – corresponding to an arrival time of a few nanoseconds. The night sky background at dark sites is typically $\sim 2 \times 10^{12}$ photons $(m^2\text{ssr})^{-1}$ (about 9 orders of magnitude smaller than the day-time sky background), so that for a typical pixels in the camera with field of view of diameter 0.2° and an effective mirror area of $\sim 60m^2$ like in H.E.S.S. (after accounting for shadowing, mirror reflectivity, Winston cone losses etc.), the night sky background is $\sim 1 \times 10^9$ photons s^{-1} , corresponding to ~ 100 MHz of photo-electron rate. For these reasons IACTs have to observe during dark night times and with extremely short exposure times of a few times $10^{-9}s$ to be able to detect the faint Cherenkov light from the shower over the night-sky background in the camera pixels. The duty cycle of these instruments is thus limited to dark nights which amounts to $\sim 10\%$. Three currently operating observatories use the stereoscopic IACT technique: H.E.S.S., MAGIC and VERITAS.

H.E.S.S. (*High Energy Stereoscopic System*) is a system of originally four (now five) IACTs located in the Khomas highland (at an altitude of 1800 m) in Namibia in southern Africa. The original four H.E.S.S. telescopes have a mirror area of $107 m^2$ with a focal length of 15m. The energy threshold at zenith is ~ 100 GeV (see Figure 5) at the trigger level. In Phase-II of the project a single very large dish with $\sim 600m^2$ mirror area and a focal length of 36m was added to the center of the array to improve the low-energy performance and to lower the energy threshold to ~ 30 GeV, significantly increasing the overlap with the *Fermi*-LAT range (4).

The MAGIC (*Major Atmospheric Gamma-ray Imaging Cherenkov Telescopes*) telescope system consists of two telescopes located on the Canary Island of La Palma at an altitude of ~ 2400 m. The two telescopes have a very large mirror area of $\sim 240m^2$, corresponding to an energy threshold of ~ 50 GeV (even down to ~ 25 GeV for special operations in so-called sum-trigger mode). They are built in a light-weight fashion to allow for fast slewing to be able to rapidly follow up on the alert of gamma-ray bursts (5)

VERITAS (*Very Energetic Radiation Imaging Telescope Array System*) is a system similar in sensitivity and performance to the H.E.S.S. phase I project, i.e. consisting of 4 IACTs with mirror size 106 m². The camera has a somewhat smaller field of view ($\sim 3.5^\circ$) than H.E.S.S.-I, but has the advantage of a very flexible trigger scheme using 500 MHz Flash-ADCs (6).

4.2.2. Water Cherenkov Detectors. Water Cherenkov detectors operate at a higher energy threshold than IACTs given that they require the shower particles to reach the ground. For that reason these detectors are typically located at higher altitudes. The total energy reaching the ground in the form of electromagnetic particles is roughly 10% of the primary energy (at 5200 m above sea level). Water Cherenkov detectors and IACTs have complementary capabilities that allow for a deeper study of the gamma-ray sky at TeV energies. Water Cherenkov detectors are typically less sensitive to point sources than IACTs (due to a combination of higher energy threshold and larger angular resolution than IACTs). However, they continuously monitor the entire sky above the detector. The solid angle surveyed by a Water Cherenkov detector is $\Omega = 4\pi \cos(l) \sin(\Theta_{max})$ where l is the latitude of the detector and Θ_{max} is the maximum zenith angle of the observation (typically 45°). For the Sierra Negra, Mexico, the site of HAWC (*High Altitude Water Cherenkov Gamma Ray Observatory*), that results in $\Omega = 2.6\pi \text{sr}$. The combination of a large field of view and nearly 100% duty cycle make them well suited to study transient sources and perform unbiased sky surveys. Also, for largely extended sources $> 1^\circ$ Water Cherenkov detectors can often be more sensitive due to the fact that IACTs typically determine the residual hadronic background from within the field of view.

Water Cherenkov detectors operate on the principle of detecting the Cherenkov light from the shower particles in the water tanks. The detector must act as an effective calorimeter to be able to suppress the hadronic background. Therefore, the PMTs need to be deep in the water, to block particles passing close to the photo-cathode of the detector and produce large pulses (that would not be proportional to the deposited energy).

The HAWC detector consists of 300 steel tanks each 4 meters high and 7.3 meters in diameter holding 188,000 litres of water. The site of the observatory is the Sierra Negra, Mexico at an altitude of 4100m. Each of the tanks contains a watertight bladder and four 8-inch PMTs, sensitive at ultraviolet wavelengths. Three of the PMTs are placed on the bottom of the tank looking upward, and spaced several meters from the center of the tank. The fourth (10-inch high-quantum efficiency) PMT is positioned in the bottom center of the tank and is intended to improve the low-energy performance. The single PMT hit rate for HAWC is $\sim 20\text{kHz}$ and the total non-correlated hit rate for the entire detector $\sim 20\text{MHz}$. Triggering is done on showers that produce > 30 PMTs hit within a $\sim 50\text{ns}$ window. The trigger rate in this regime corresponds is 5 – 10kHz. The background rejection (at a fixed gamma-ray efficiency of 50% is a function of energy and improves from 10% at 500 GeV to a few times 10^{-3} at above 10 TeV.

5. Science Discoveries

Our understanding of the gamma-ray sky has evolved and improved over the last decade. The combination of instruments such as the *Fermi*-LAT and AGILE at GeV energies and ground-based observatories IACTs such as H.E.S.S., MAGIC and VERITAS coupled with Water Cherenkov detectors such as MILAGRO and now HAWC have ushered an era of both

FGST: <i>Fermi</i> Gamma-ray Space Telescope
Fermi-LAT: <i>Fermi</i> Large Area Telescope
H.E.S.S.: High Energy Stereoscopic System
MAGIC: Major Atmospheric Gamma-Ray Imaging Cherenkov Telescopes
VERITAS: Very Energetic Radiation Imaging Telescope Array System
HAWC: High-Altitude Water Cherenkov Observatory
CTA: Cherenkov Telescope Array

significant increase in the number of sources as well as a significantly improved understanding of the most prominent members of the various source classes. In general, all sources of GeV and TeV gamma rays are either locations of high-energy (non-thermal) processes or are indication of locations of new physics in the Universe beyond the standard model of particle physics.

The image of the GeV sky (Figure 1) illustrates three main components of the gamma-ray sky: a) Galactic diffuse emission, generated by the interaction of the pool of CRs in our Galaxy with interstellar gas and radiation fields, b) individual sources, and c) a faint glow of isotropic diffuse emission, detectable at all Galactic latitudes. The relative contribution of these sources to the total gamma-ray flux changes with increasing energies. While at GeV energies about 80% of all photons are Galactic diffuse emission, at TeV energies individual sources dominate since the source spectra are typically harder (meaning more high-energy photons) than the Galactic diffuse emission. The latter follows the spectrum of the pool of CRs which exhibits a power-law in energy with a photon index of $\Gamma = 2.7$ and therefore dominates mostly at low energies. The Galactic diffuse emission is, however, also detected at TeV energies by H.E.S.S. in the innermost part of the Galaxy (see discussion below) and also by MILAGRO in a large-scale region on the Galactic plane. Also recently, the deep H.E.S.S. observations of the Galactic plane survey (57, 58) allowed for the first time to detect a large-scale gamma-ray emission along the Galactic Plane using IACTs. This and the MILAGRO detection at TeV energies could thus either have a CR-induced origin or could be due to unresolved source populations or a combination thereof. The Galactic diffuse emission generally provides very important information about the propagation and diffusion of CRs and additionally on interstellar radiation and gas fields.

One of the most important discoveries in recent years both at GeV and TeV energies was the variety of source classes with which the gamma-ray sky is populated. Quite generally, given that most energy spectra are powerlaws that decrease rapidly with increasing energy the expectation is that for instruments with similar flux sensitivities (as is the case with current ground and space-based instruments) the numbers of sources at low energies will exceed the number of sources at high energies. With ground-based instruments about 148 sources have been discovered both galactic and extragalactic in origin (see e.g. Figure 1) above $\sim 100\text{GeV}$. At GeV energies the third *Fermi* LAT gamma-ray source catalog (59) (based on the first four years of observations) lists more than 3000 galactic and extragalactic gamma-ray emitters (see Figure 1). Out of the 148 TeV sources a large fraction (117) are also detected at GeV energies by *Fermi*-LAT. On the extragalactic sky all but one of the 58 TeV AGN are detected with *Fermi*-LAT (only HESS J1943+213 does not have a 3FGL counterpart). This TeV blazar is unique in that it is located on the Galactic plane and therefore in a region of reduced sensitivity for *Fermi*-LAT.

For both the GeV and the TeV sky, the identification of gamma-ray emitting regions with astrophysical counterparts is an important topic. Quantitatively, the 3rd *Fermi*-LAT catalog lists about two-thirds of the detected objects as positionally coincident (i.e. *associated*) with counterparts representing known source populations (more than two hundred thirty sources firmly identified based on the angular extent or the temporal behaviour), the origin of approximately one-third of these objects remains an open issue. The same is true for the TeV sky. The limited angular resolution and (at least on the GeV sky) the bright diffuse emission from the pool of Galactic CRs makes source confusion in the Galactic plane a serious issue. The most reliable approach for the identification of gamma-ray sources is the analysis based on temporal studies. In this regard, the best “astronomical clocks” - the

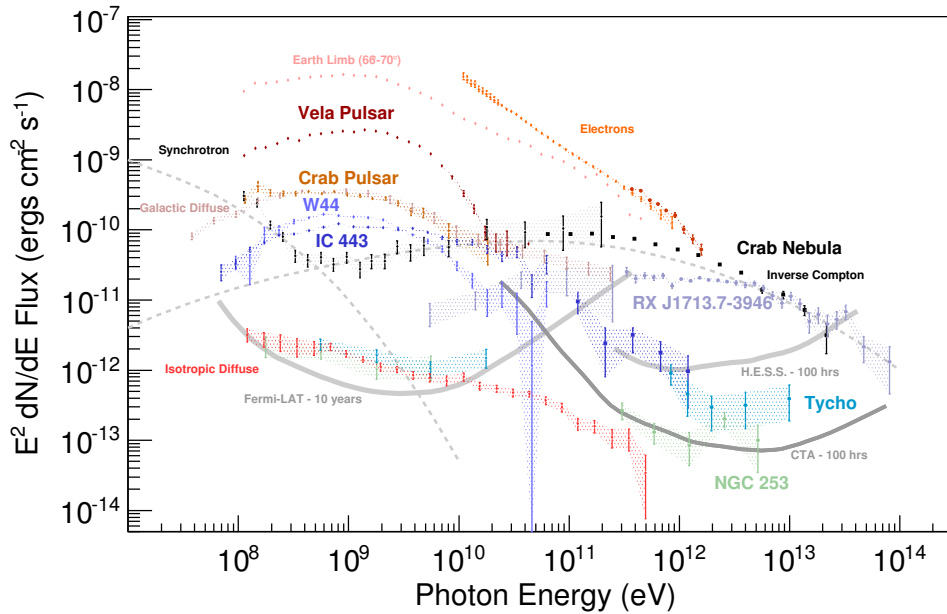


Figure 6

Spectra for a selected number of GeV and TeV sources – both for point-like and diffuse sources (for the diffuse sources the solid-angle has been converted to a field of view of a typical ground-based instrument of 5°). Also shown are the *Fermi*-LAT, H.E.S.S., and CTA differential sensitivity for 4 bins per decade.

pulsars - constitute the largest population of identified Galactic gamma-ray sources (more than 120) in the GeV band. The spectra of pulsars do however typically show a break in the multi-GeV region so that a detection at TeV energies becomes extremely difficult and only possible for the brightest objects, such as the Crab pulsar and the Vela pulsar. At TeV energies, the largest number of detected Galactic sources are pulsar wind nebulae (PWN) that ultimately also convert the pulsar rotational energy into electromagnetic radiation. The periodic character of gamma-ray emission of the Galactic binary systems or the sporadic flares of AGN provide another tool for identification of variable gamma-ray sources based on simultaneous observations in different energy bands. Given the very large number of unidentified sources both at GeV and TeV energies, interesting (and unexpected) physics might be waiting to be discovered.

Instead of giving a laundry list of all the sources discovered and the important science topics covered in their interpretation, in the following, I will highlight two of the most important science cases for gamma-ray astronomy: the origin of CRs and the search for dark matter.

5.1. The Origin of Cosmic rays

All gamma-ray sources are potential sources of CR protons. Gamma rays therefore can be used to trace the populations of energetic particles in SNRs. The flux of hadronic gamma

rays is governed by the CR density and the target gas density. The flux of leptonic gamma rays is traced by the electron density and the radiation fields (which are usually assumed to be constant on the scale of the source). To distinguish the sources of CR protons from the sources of CR electrons, gamma ray observations are often not sufficient but multi-wavelength observations have to be taken into account. These observations – mostly at radio and X-ray energies – indicate that for the best candidate sources for the origin of Galactic CRs – SNRs – ultra-relativistic electrons and large magnetic fields (beyond $100 \mu\text{G}$ for several of the young SNRs) are present in the shocks. If indeed large magnetic fields are present in SNR shocks, the two conclusions that can be drawn are: a) the gamma-ray emission is probably hadronic in origin, since the electron density needed to explain the synchrotron flux is rather low, b) the best-understood way to enhance or amplify the magnetic field in SNR shock front is through the pressure of accelerated protons. This so-called streaming instability of upstream CRs in a parallel shock (60, 61) is a matter of active research and its existence has strong implications for the maximum energy achievable in SNR shocks. Young SNRs that show indication of large magnetic fields are ideal targets to search for gamma-ray emission that is hadronic in origin and for sources of CRs up to very high energies – possibly even close to the knee in the spectrum of CRs at 10^{15} eV. SNRs for which the shock wave is encountering a region of dense interstellar material such as a molecular cloud can be expected to have a high flux of hadronic gamma rays.

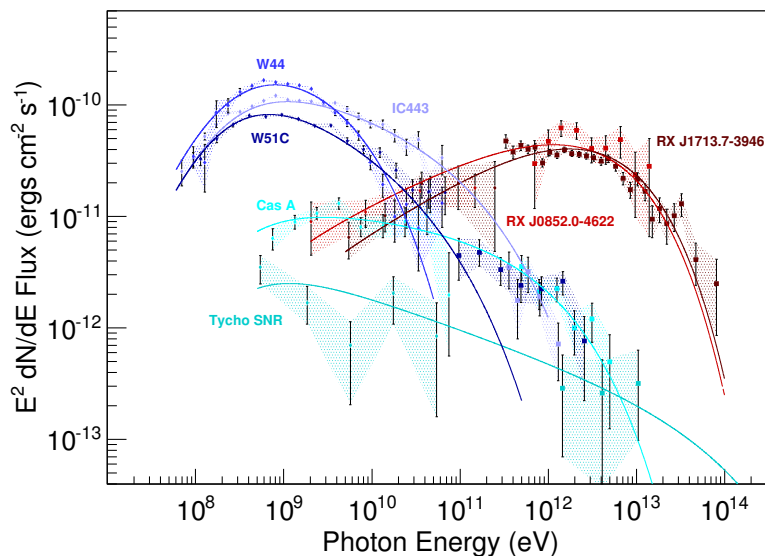


Figure 7

Typical gamma-ray energy spectra for several of the most prominent SNRs. Young SNRs (< 1000 years) are shown in cyan. These typically show smaller gamma-ray fluxes but rather hard spectra in the GeV and TeV band. The older (but still so-called young) shell-type SNRs RX J1713.7–3946 and RX J0852.0–4622 (Vela Junior) of ages ~ 2000 years are shown in red colors. These show very hard spectra in the GeV band ($\Gamma = 1.5$ and a peak in the TeV band with an exponential cutoff beyond 10 TeV). The mid-aged SNRs ($\sim 20,000$ years) interacting with molecular clouds (W44, W51C and IC443) are shown in blue. Also shown are hadronic fits to the data (solid lines).

Indeed, beyond pulsars and PWNe (which are generally assumed to be dominated by CR electrons) the largest number of detected gamma-ray sources in the Galaxy are SNRs. The *Fermi*-LAT team is about to release its catalog of SNRs in which the data are analysed for each of the known SNRs (62) in our Galaxy, resulting in approximately 40 detections. For these detections two classes emerge (see e.g. Figure 7): the largest class in the GeV-detected SNRs are those known to be interacting with molecular clouds such as IC443, W44 and W51C (see Figure 8). The second class are young SNRs that are typically less luminous at GeV energies, have harder spectra and are often also detected at TeV energies. At TeV energies 11 shell-type SNRs are detected, including such objects like Tycho’s SNR, Cas A, SN 1006 and RX J0852.0–4622 (Vela Junior) as well as RX J1713.7–3946 (see Figure 9). The results seem to indicate that the CR efficiencies ϵ_{CR} (the efficiency of converting the SN explosion energy into CRs) are broadly consistent with a value of 10%, albeit with rather large errors for individual SNRs due to uncertainties about distance, explosion energy and target density surrounding the remnants (63). A study at TeV energies with H.E.S.S. based on the Galactic plane survey (57, 58) came to similar conclusions (64).

5.1.1. Supernova remnants interacting with interstellar material. This is the largest class of GeV-detected objects and the brightest SNRs IC443, W44 and W51C are the brightest objects of this class on the GeV sky (see Figure 7). The brightness stems from the rather large density of target material stemming from the interaction of the shock wave with surrounding molecular clouds (up to $n = 1000\text{cm}^3$). For these objects a correlation between the GeV and the radio flux seems to emerge (69) indicating non-thermal emission from relativistic particles. For IC 443 and W44, the characteristic low-energy cutoff in the energy spectrum (“pion bump”) has been detected (70, and see Figure 7), clearly demonstrating that the gamma-ray emission in the GeV band is dominated by π^0 -decay and therefore unambiguously proving that CRs protons are accelerated in the shock waves of Supernova remnants. This measurement provides an important step forward in relating SNRs to the origin of CRs. The gamma-ray spectra of these (mid-aged, i.e. $> 10,000$ years) objects also show a high-energy break at around 2 GeV (for W44) and 20 GeV (for IC443) well short of the knee in the spectrum of the CRs. At this point it is unclear, whether this high-energy break is related to the age of the SNRs, to Alfvén damping in a dense environment (71), to the velocity of scattering centers responsible for the particles diffusion around the shock (72) (this would change the compression factor) or to the effects of escape from the remnant (73). While W44 is so far not detected at TeV energies, IC 443 has been detected with rather soft energy spectrum both by MAGIC (67) and by VERITAS (74). For IC 443 the centroids of the GeV and TeV emission are not coinciding, a fact that could be explained as the result of the escape of high energy CRs from the SNR shell and of their interaction with the ambient medium. In this scenario, the diffusion coefficient for the multi-TeV CRs is of the order of $D \approx 10^{27}(\epsilon_{CR}/0.1)^2 \text{ cm}^2/\text{s}$ (with ϵ_{CR} the efficiency of converting the SN explosion energy into CRs), a diffusion coefficient that is much smaller than the average diffusion coefficient in the Galaxy (75). While these measurement provide an important proof of the acceleration of CR protons in shock wave of SNRs, the lessons that can be learned on the acceleration of the bulk of CRs in our Galaxy are somewhat limited since the maximum particle energy is way short of the “knee” in the spectrum of CRs. In this respect the second class of objects – the young SNRs are much more important.

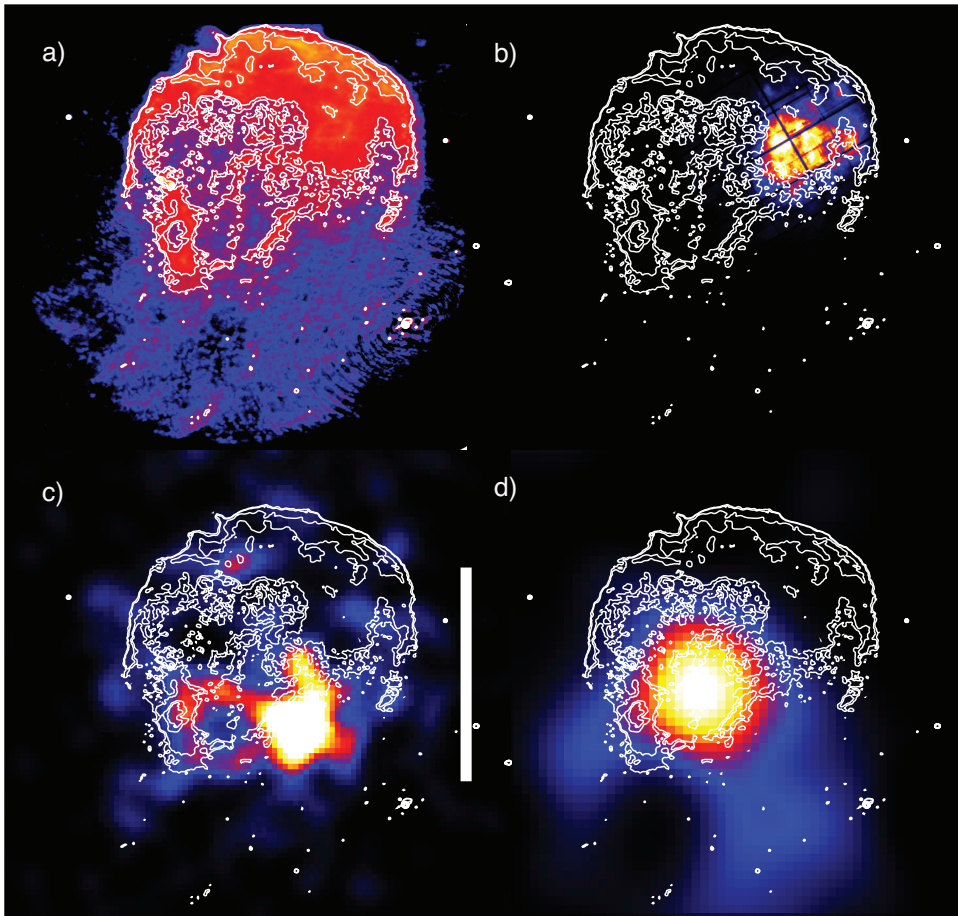


Figure 8

Multiwavelength data for SNR IC443 in Galactic coordinates. The white bar is 0.4° long. Data are taken from: a) VLA 330 MHz continuum emission (fits image kindly provided by Dr. Gabriela Castelletti) (65), b) XMM observations (0.3-8 keV) (66), c) GeV gamma rays observed by *Fermi*-LAT above 10 GeV (source class, 6.5 years of data) smoothed counts d) MAGIC observations above 380 GeV (67).

5.1.2. Young Supernova remnants. Young SNRs are the prime candidates for acceleration of protons to very high energies. If one assumes that shock acceleration is universal, the emission from these objects into gamma rays and whether the emission is predominantly leptonic or hadronic in origin is strongly influenced by the environment (i.e. the density of interstellar material and of radiation fields in the shock region). The most prominent of the young SNRs that have been detected both at GeV and TeV energies are RXJ J1713.7–3946 (1, 76), Tycho’s SNR (77, 78), and Cas A (79, 80, 81, 82, 83). The situation for RX J1713–3946 (and its companion TeV shell-type SNR RX J0852.0–4622) – arguably the most-discussed case of a gamma-ray emitting SNR and the brightest object of its class at TeV energies – is rather complicated. The spectral shape measured over a large energy range

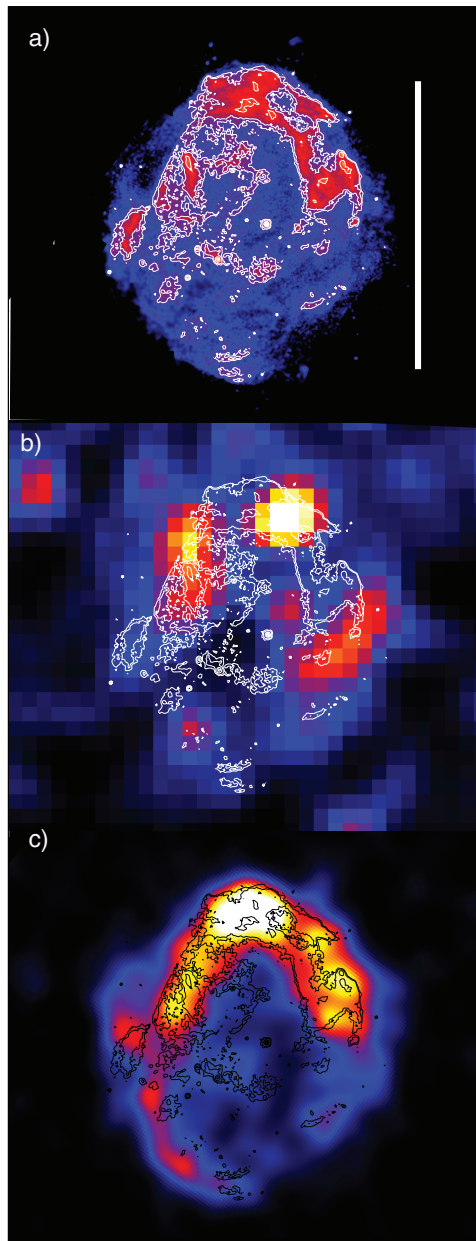


Figure 9

Multiwavelength data for SNR RX J1713.7-3946 in Galactic coordinates. The white bar is 1° long. Data are taken from: a) XMM-Newton observations (68), c) GeV gamma rays observed by *Fermi*-LAT (source class, 6.5 years) d) H.E.S.S. observations (1).

with *Fermi*-LAT and H.E.S.S. from $\sim 1\text{GeV}$ to $\sim 100\text{TeV}$ suggests a leptonic origin of the gamma-ray emission due to the rather hard photon index $\Gamma = 1.5$ in the GeV range (76,

and see Figure 7). In addition, the absence of thermal X-ray emission which is expected in hadronic scenarios, even for a case in which electron heating proceeds very slowly suggests very severe upper limits on the density of gas in the shock region (84). This suggests that the region lacks the target material for the interaction of potentially accelerated protons to produce neutral pions further supporting the leptonic scenario. However, (85) pointed out that the expectations for the hardness of the spectrum and for the thermal X-ray emission can change strongly if assuming a non-uniform (clumpy) structure of gas density around the SNR (as expected if the progenitor is a massive star in a molecular cloud). In this case the diffusion of CRs into the clumps might be such that only the highest energy CRs can penetrate into the center of the clumps and therefore the proton spectrum “seen” by the gas target might be extremely hard and therefore produce a very hard gamma-ray spectrum (see also 86, for a comprehensive discussion). Whether the requirements on the clumpiness of the medium and the density in the clumps is met in RX J1713.7–3946 is still a matter of active debate. The number of clumps in this scenario needs to be sufficiently large (of the order of 1000) to make the gamma-ray emission spatially smooth. If the gamma-ray emission is indeed caused by accelerated hadrons the maximum energy of the protons is ~ 150 TeV (85). Such hadronic scenarios can not be ruled out with current data but require multi-zone modelling of the emission region (which in fact fit the observed parameters rather well as e.g. shown in 86). It should be noted that also in the case of one-zone leptonic models problems exist. The required density of the IR light necessary to explain the H.E.S.S. data is significantly (about a factor of ~ 25) larger than expected. Also, the one-zone leptonic model requires magnetic field strengths of the order of $\sim 10\mu G$, far too low to explain the sharpness of the X-ray filaments (with electron cooling) and the observed short-term (yearly) variability of the hard X-ray emission. So it seems, that also for the leptonic emission a multi-zone model is necessary to explain all the observational data. The future will provide more sensitive observations of the thermal X-ray emission with Astro-H of this object (87) and ultimately, the detection of ultra-relativistic neutrinos from this object might be necessary to unambiguously distinguish between the different scenarios. Clearly, gamma-ray observations with the Cherenkov Telescope Array (CTA) will provide significantly higher angular and spectral resolution studies for this object. From the current observational data it seems clear, however, that this object is located in a very complex environment and disentangling the environmental parameters from the acceleration properties will be a challenging task also in the future.

The cases of Tycho and Cas A might be clearer (see Figure 7). For these, the gamma-ray spectrum continues with a spectral index of $\Gamma = 2.0$ from the high-energy TeV range observed by VERITAS (77) into the lower-energy GeV region, thereby matching more the expectation from a hadronic scenario and diffusive shock acceleration (88, 89). In particular Tycho’s SNR, resulting from a historical Type Ia progenitor supernova explosion expanding into an undisturbed and therefore more uniform interstellar medium, seems to be a very good case for the hadronic interpretation of the broad-band gamma-ray emission. Like in the case of other SNRs the thin X-ray rims suggest large magnetic fields in the shock region ($\sim 300\mu G$) suggesting a maximum energy of accelerated protons of up to ~ 500 TeV (88). A similar case for hadronic emission can be made for Cas A, for which the gamma-ray spectra seem to suggest two energy breaks, one at low energies (~ 1.5 GeV resulting in a very steep index below that energy, again consistent with a pion-bump (82, 83). In the energy range between the *Fermi*-LAT measurements and the measurements of MAGIC (81) and VERITAS (80) an additional steepening is necessary. If this steepening indicates a cutoff in

the energy spectrum of the gamma rays efficient particle acceleration in Cas A to very large energies is at least questionable (89). Recent *NuSTAR* hard X-ray data (3–79 keV) suggest that the GeV emission is spatially not associated with the bright features in the hard X-ray band while the TeV emission may be. While the angular resolution of the gamma-ray data might not be sufficient at this time to unambiguously make this claim, such a measurement might suggest that in the gamma-ray emission in Cas A both hadronic and leptonic emission mechanisms may be at work (90).

An interesting case is the other two young SNRs RCW 86 and SN 1006 (both of age ~ 1000 years). Both of them are detected at TeV energies in deep H.E.S.S. observations (91, 92) and both of them show no emission in the GeV range (in the case of SN 1006) or extremely faint emission (in the case of RCW 86). These observations put rather stringent constraints on the spectral index of the protons in a hadronic scenario and limits them to be significantly harder than $\Gamma = 2$ (93, 94). In the case of RCW 86 a recent detection with *Fermi*-LAT determines the spectral index to be $\Gamma = 1.4$ (95). Similar to the case of RX J1713.7–3946, these observations favor a leptonic model if one assumes a one-zone model with a uniform density. All the complications described above for RX J1713.7–3946 might also apply to these remnants.

Summarising the situation for young SNRs: while the situation in RX J1713–3946 remains complex probably due to the complex environment in which the remnant propagates the cases for Tycho SNR and Cas A seem to be more clearly indicating predominantly hadronic emission with typical efficiencies for converting explosion energy into the acceleration of CRs of the order of 10%. Measuring the spectra of these remnants to the very highest energies and determining the shape and presence of energy cutoffs with CTA will provide important additional constraints on the acceleration processes.

5.1.3. Cosmic rays diffusing away from the sources. If a molecular cloud is located in the vicinity of the acceleration region the diffusion of CRs can be studied. Depending on the spatial location of the molecular cloud and the accelerator different signatures are expected. The energy dependence of the diffusion coefficient of the CRs typically alters their spectrum from the source to the interaction region. This in turn affects the spectral shape of the gamma-ray emission in the cloud and in the accelerator. Measuring wide-band spectra of accelerator and cloud can therefore help to constrain the diffusion coefficient in these regions.

One of the most prominent targets for the study of diffusion of CRs in our Galaxy is the Cygnus region. Cygnus was detected both at GeV energies (96) and at TeV energies (97, 98, 99, 100). In the Cygnus region, *Fermi*-LAT detected an extended excess of gamma-ray emission, the so called *Fermi cocoon*, which seems to be related to the combination of many powerful SNR and stellar-wind shocks. Recently the ARGO Collaboration claimed the association of the source ARGO J2031+4157 with the cocoon (100), and which provided a connection between the spectrum of the cocoon measured by *Fermi*-LAT with that of the Milagro source MGRO J2031+41. The spectral index of the gamma-ray emission when combining these measurements is $\Gamma = 2.16$ with a cutoff at $E_c = 150\text{TeV}$. The detection of hard extended emission above 1 GeV towards the central part of Cygnus X is spatially coincident with a cavity in the interstellar medium blown by the winds and ionisation fronts from Cyg OB2, NGC 6910 and other massive stellar clusters (96). The hard spectrum of this emission is inconsistent with e.g. local CR emissivities and has therefore been interpreted as the signature of freshly accelerated particles. The scale of this region is $\sim 50\text{pc}$, the

total luminosity in gamma rays above 1 GeV represents however only a modest fraction (0.03%) of the mechanical wind power in the stellar winds of Cygnus OB2. This discovery seems to confirm a long-standing hypothesis that massive-star forming regions can accelerate particles to relativistic energies. Additionally, it provides an observational test case to study the escape of CRs from their sources and the impact of wind-powered turbulence on their early evolution.

Another important class of observations has been made for regions surrounding shell-type SNRs, such as W28, and W44. In W44 CRs escaping from the SNR region and interacting with molecular clouds in the vicinity of the remnant have been observed in the GeV range with the *Fermi*-LAT (101). Also for W28 gamma-ray emission from surrounding clouds has been detected both at GeV (102) and at TeV energies (103). The TeV emission coincides well with the position of the three most massive molecular clouds. One of these is interacting with the SNR shell (HESS J1801-233) while the other two are located outside of the SNR (HESS J1800-240A and B). A joint fit to all three suggests that the diffusion coefficient in this region is much smaller (by up to 2 orders of magnitude) than that in the Galaxy as a whole – a result consistent with the measurements in IC 443. It should however be noted, that for all these objects the uncertainty about the age, distance and three-dimensional relation between the acceleration region and the clouds makes the conclusions somewhat uncertain. If indeed the diffusion coefficient is severely suppressed around SNRs, it might be related to an enhancement in the magnetic turbulence surrounding the remnant due to CRs streaming away from the source.

Finally, on a larger scale the *Fermi bubbles* can be used to study the diffusion of particles (see discussion below) if indeed they are related to hot outflows powered by activity of the supermassive black hole in the Galactic center (104, 105, 106, 107, 108, 109, 110).

5.1.4. Maximum energy in Cosmic rays. The maximum energy attainable in SNR shocks is directly related to the magnetic fields that confines the particles at high energies to the shock area. In a recent investigation (111) assumed that escaping CRs trigger magnetic field amplification through streaming instabilities. They estimated the number of particles escaping as a function of shock velocity and SN type (ambient density). They concluded that young SNRs reach ~ 200 TeV energies for shock velocities of $v_{sh} = 5000$ km/s. Using the observed properties of Tycho, SN 1006 and Cas A, the authors determine E_{max} to be 100 TeV, < 60 TeV, and 280 TeV respectively, largely consistent with the gamma-ray observations. The authors conclude that the highest energies for CRs are reached in the very early phases of SNR evolution, especially in the core-collapse SNe in a dense wind, which are representative for the early stages of most type II SNe. PeV energies are then reached only in the first few hundred years and only in a dense wind environment. For the known Galactic SNRs, Cas A seems to be the best candidate to have been an accelerator to the knee, although only in the early stages of its evolution and now no more. It seems plausible that younger SNRs with even higher shock velocities can accelerate particles up to the knee – however, the question is whether these SNRs have swept up enough material and accelerated enough material to account for the total flux of CRs seen at Earth. Nevertheless, the absence of a Pevatron at this time does not seem to pose a major problem to the paradigm of diffusive shock acceleration in SNR shocks, given that these Pevatrons possibly operate for only a very short period of time (112, 113).

Interestingly, there seems to be a second population of CRs in SNRs, those that do not have enough energies to escape before the end of the lifetime of the shock wave. CR with

energies up to ~ 200 GeV are confined to the SNR for the lifetime of the SNR and form a CR bubble that gets released into the Galaxy only at the end of the SNR's life (see e.g. 114). These bubbles might not be strong emitters of gamma rays due to the low gas densities in the bubbles. The recently discovered *Fermi* bubbles might be related to this phenomenon.

5.1.5. Cosmic rays in other galaxies. We know that the GeV gamma-ray emission of our Galaxy is dominated by the interaction of CRs with interstellar material. Whether this is true also for other galaxies remains a matter of active study. So far, also the Large Magellanic Cloud (LMC) (115) and the Small Magellanic Cloud (SMC) (116), M31 (117) as well as several active star forming Galaxies (most notably M 82 and NGC 253) (118, 119) have been detected at GeV and TeV energies. For NGC 253 the gamma-ray spectrum can be described by a power law with photon index $\Gamma = 2.2$ from 200 MeV to 5 TeV (118, 120, 121). Active star formation leads to an enhanced rate of Supernova explosions and therefore to an enhanced CR density. Basic considerations suggest that the timescales for the acceleration of CRs and subsequent energy loss (via pion-decay, or advection by bulk outflows) are shorter than the timescales of starburst activity in Galaxies. Consequently, a balance is expected between energy gains and losses for Galactic CRs in a burst of star formation. In a population study of 64 close-by galaxies selected by their abundant molecular gas, a 3-year data analysis of *Fermi*-LAT data revealed a clear (quasi-linear) scaling relation between gamma-ray luminosity and both radio continuum luminosity and total infrared luminosity. In the paradigm that SNRs channel approximately 10% of their mechanical energy into CR nuclei with kinetic energies > 1 GeV, the normalisation of the observed scaling relation between gamma-ray luminosity and star-forming rate implies that starburst galaxies have an average calorimetric efficiency for CR nuclei of 30-50% if the gamma-ray emission is dominated by neutral pion decay (119). Interestingly, the rather hard gamma-ray spectra ($\Gamma = 2.2 - 2.3$) of starburst galaxies such as NGC 253 (121) and M82 (122) suggest energy-independent loss mechanisms for CR nuclei in starbursts, as opposed to the diffusive losses which likely shape the observed gamma-ray spectra of the Milky way and the other quiescent Local Group galaxies (such as the LMC, SMC). These energy-independent loss mechanisms could include hadronic interactions but also advective transport of CR nuclei in starburst galaxies. The overall normalisation of the relation between gamma-ray luminosity and star formation rate ultimately supports the understanding that the majority of CR energy in most galaxies eventually escapes into intergalactic space losing only a few percent of their energy through pion production and ionisation in Milky Way-like galaxies (123). Star-forming galaxies have more gas and possibly heavier losses, yet for the detected objects galaxies M82 and NGC 253 still 60-80% escape (likely in a wind) (see e.g. 124, 121, 119) into the intergalactic medium. Here they build up over the Gyrs of cosmic star formation. (125) has shown, that CR can couple to the intergalactic medium and its weak magnetic field and ultimately can reach a density within a factor of a few of the Ly α forest pressure, probably having the strongest effect at redshifts of $z \sim 1$ and larger, when the star-formation was largest and most of the intergalactic medium was cool.

5.2. The Search for Dark Matter

Because of the quadratic dependence of the self-annihilation rate on the dark matter density the detectability of any particular region in the Universe (see equation 4) strongly depends on the density distribution of dark matter particles along the line of sight (so-called J-factor).

Unfortunately, dark matter densities are not very well constrained by numerical simulations, especially in the innermost regions of Galaxies. In fact, simulations originally showed that the collapse of cold dark matter gives rise to rather cuspy dark matter haloes (something that would favor the indirect detection of dark matter because of the ρ_{DM}^2 dependency). On the other hand, observations of galaxy rotation curves favor constant density cores (so-called ‘cusp-core problem”, (see e.g. 126, 127, 128). An additional complication stems from substructure in the dark matter distribution that is currently not resolved in cold dark matter N-body simulations, (i.e. below $\sim 10^5 M_{\odot}$). This unresolved substructure can have a very large impact, in particular in objects such as galaxy clusters. Since substructure will further enhance the annihilation signal this effect is typically quantified in terms of the so-called boost factor B defined as the ratio of the true line-of-sight integral to the one obtained when assuming a smooth component without substructure. Finally, the situation is further complicated by the fact that for many objects (such as e.g. the Milky Way) baryonic matter dominates the inner parts of the gravitational potential. Baryons are expected to have a significant impact on the dark matter profile compared to the numerical simulations which are generally dark matter-only. The infall of baryons is expected to alter the inner dark matter profiles. The profile could either be steepened through adiabatic contraction (129, 130), or it could be flattened through the occurrence of repeated star bursts triggered by baryonic infall which tends to render the gravitational potential shallower since the star burst activity drives out the baryons from the inner parts (131, 132).

The choice of the assumed profile of the density distribution constitutes therefore one of the prime uncertainties in studying dark matter using gamma rays. The resulting uncertainties on the expected flux limits for individual dwarf spheroidals are between a factor of 3 for well-constrained objects like Sculptor up to a factor of 10 for objects such as Coma Berenices. For the center of our Galaxy, arguably the most promising target in terms of expected gamma-ray flux from dark matter annihilations, these uncertainties are considerably larger. (See 133) for a discussion on the dark matter profile in the inner Galaxy from a meta-analysis of kinematic data of the Milky way. Estimates can differ by up to a factor of 50 depending on the choice of the profile. For clusters of galaxies the main uncertainties come from the treatment of substructure below the resolution limit of current numerical simulations. Also here, the uncertainties in the J-factor can be several orders of magnitude, and the dark matter profile itself can be severely modified in these objects by the presence of substructures.

No unambiguous evidence of gamma rays from dark matter annihilation has been detected so far (see a discussion of the Galactic center later). Therefore, upper limits on the annihilation cross sections (under the assumptions of certain dark matter profiles) have been derived for various objects. Interestingly, many of these upper limits especially in the GeV range already touch on physically meaningful parts of the dark matter parameter space. In particular reaching the thermal relic cross section in the stacking of dwarf spheroidal Galaxies with the *Fermi*-LAT should be noted. The various sources for which upper limits have been derived will be discussed in the following:

5.2.1. Dwarf Spheroidals. In contrast to the aforementioned uncertainties in the inner parts of the density profile of objects on Galaxy or galaxy cluster scales, dwarf spheroidal galaxies can represent a very clean system to search for dark matter annihilation. Indeed, star formation is usually very much suppressed in these objects, so astrophysical foregrounds that produce gamma rays are less of an issue in these objects. Boost factors through substructure

below the resolution of numerical simulations are expected to be irrelevant in these objects and therefore do not add a large uncertainty. Uncertainties related to the shape of the dark matter profile are generally integrated over and are at the 10-50% level. Currently, there are roughly 25 known dwarf satellite galaxies to the Milky Way and ground-based instruments such as H.E.S.S., MAGIC and VERITAS as well as the *Fermi*-LAT are actively observing these objects. While none of the objects are detected with the current generation of gamma-ray instruments, important conclusions on the properties of dark matter particles can be drawn from these objects. In particular, a combined analysis of all known dwarf satellites with the *Fermi*-LAT have pushed, for the first time the annihilation interaction rate limits below the canonical thermal relic production cross-section of $3 \times 10^{-26} \text{cm}^3 \text{s}^{-1}$ for a range of WIMP masses (around 10 GeV) for the annihilation into $b\bar{b}$, which often acts as a benchmark (134, 135). This statement holds also if uncertainties in the J-factors for these objects are included. Given the all-sky capability of the *Fermi*-LAT, a combined analysis of these objects will remain the cleanest target in the future where more dwarfs are expected to be detected with future optical surveys such as Pan-STARRS (136), DES (137) and LSST (138). Estimates show that DES might discover 19 to 37 new dwarf galaxies during the duration of the *Fermi*-LAT mission (139). At higher energies ground-based IACTs have also observed dwarf spheroidals but have not found a signal (140, 141, 142). Their limits for high WIMP masses are typically several orders of magnitudes away from the thermal relic interaction rate and are therefore not (yet) competitive with limits from the *Fermi*-LAT at lower energies.

5.2.2. Galaxy Clusters. Galaxy clusters are more distant than dwarf spheroidal galaxies or any of the other targets that are generally used for dark matter studies using gamma rays. However, similar to the case of dwarf spheroidals, they are expected to be dark matter dominated. The range of proposed boost factors due to unresolved dark matter substructure can be large. Depending on the assumption about the substructure galaxy clusters become competitive in their expected annihilation signal with dwarf spheroidals only at the extreme (high) end of boost factors. The best candidate are massive nearby clusters such as Virgo, Fornax or Coma (143, 144, 145). One complication for a possible detection is that galaxy clusters are also expected to contain a significant number of astrophysical sources of gamma rays, such as Active Galactic Nuclei (AGN) or radio galaxies. In addition, these objects are expected to harbor a significant population of CRs which should radiate gamma rays through interaction with hadronic material and subsequent pion-decay. *Fermi*-LAT has not detected any signal from a cluster of galaxies, and as long as no signal is found, ignoring the CR contribution represents a conservative assumption and is therefore justified (146, 147, 148, 144). At higher energies ground-based instruments have pushed for rather stringent gamma-ray flux limits on galaxy clusters (e.g. the MAGIC telescopes for the Perseus cluster (149), the VERITAS array for the Coma cluster (150), and the H.E.S.S. array for the Fornax cluster (151)). However, when making conservative assumptions about boost factors in these objects, the limits on the benchmark $b\bar{b}$ annihilation channel are several orders of magnitude away from the canonical thermal relic interaction rate.

5.2.3. Isotropic diffuse emission. The *Fermi*-LAT has provided a measurement of a faint diffuse isotropic signal (IGRB) from 100 MeV to 820 GeV (152). Due to the large-scale structure of the signal and the inability to reject the electron background, this emission

is not detectable with ground-based detectors. The isotropic emission exhibits a power law with index $\Gamma = 2.32 \pm 0.02$ with a significant exponential cutoff at 279 ± 52 GeV – a statement that is robust against changes in the Galactic diffuse foreground model. At an energy of 100 GeV, roughly half of the total IGRB intensity has now been resolved into individual sources by the LAT, predominantly blazars of the BL Lacertae type. The cutoff in the energy spectrum can in principle be explained by a single dominant extragalactic source population with EBL attenuation (152, 153, 154). This signal is expected to contain a contribution of mainly extragalactic unresolved (sub-threshold) sources combined with potentially truly diffuse emission. It is thus possible that the IGRB emission contains the signature of some of the most powerful and interesting phenomena in astroparticle physics. Intergalactic shocks produced by the assembly of Large Scale Structures (155, 156, 157), gamma-ray emission from galaxy clusters (158, 159), emission from starburst and normal galaxies (160, 161), are among the most likely candidates for the generation of diffuse GeV emission. In addition, a signal from dark matter annihilation could be imprinted in the IGRB. While it would be extremely difficult to detect a dark matter contribution in the IGRB, upper bounds on dark matter annihilation can be readily derived. The most conservative approach when calculating upper limits on the dark matter annihilation interaction rate is to assume that all of the IGRB is caused by dark matter annihilation. When making rather conservative assumptions about the contribution of source populations to the IGRB dark matter annihilation interaction rate limits can be derived (162, 163, 164, 165) that are competitive with other methods, such as dwarf spheroidal galaxies. Obviously, these limits can be significantly tightened when including additional source populations – however, the degree to which the contribution from such classes can be determined is questionable.

The statistical properties of the IGRB additionally encodes information about the origin of this emission. Unresolved sources are expected to induce a different level of small-scale anisotropies compared to truly diffuse contributions. A study of the angular power spectrum of the diffuse emission at Galactic latitudes $|b| > 30^\circ$ between 1 and 50 GeV revealed angular power above the photon noise level at multipoles $l > 155$ independent of energy (166). The scale independence of the signal suggests that the IGRB originates from one or more unclustered populations of point sources. The absence of a strong energy dependence suggests that a single source class that provides a constant fractional contribution to the intensity of the IGRB over the energy range considered may provide the dominant contribution to the anisotropy. Recently it has been suggested that a strong correlation between cosmic shear (as measured by galaxy surveys like DES and Euclid) and the anisotropies in the IGRB might add an additional handle on the contribution of dark matter annihilation to the IGRB (167).

Figure 10 summarises the current status of dark matter limits from various objects.

6. Future prospects

The supplemental material gives a detailed account of one of the most exciting regions on the sky: the Galactic center and its complex interplay between cosmic ray sources, gamma-rays from propagating cosmic rays, and dark matter. As described there, given the complexity of the emission region it is difficult to draw unambiguous conclusions and future observations will be needed to improve the picture. In the absence of a space-mission that would improve the overall sensitivity over the *Fermi*-LAT by an order of magnitude in the

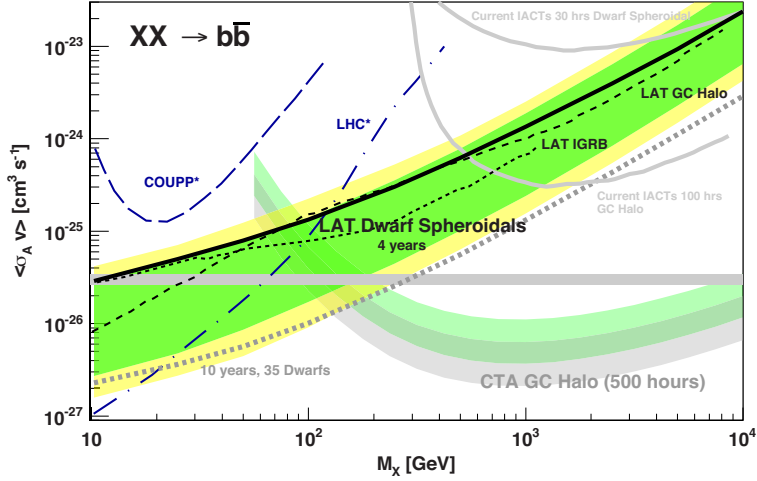


Figure 10

Reproduced from (24). Compilation of current limits from the *Fermi*-LAT on dark matter annihilation interaction rate σv using gamma rays, along with projected future limits from the Cherenkov Telescope array (CTA). Also shown are limits from direct detection (COUPP (168)) and accelerator experiments (LHC ATLAS (169) and CMS (170)) transformed to limits on the annihilation cross section on the assumption of four-particle contact interactions as in (171). The *Fermi*-LAT limits were taken from the *Fermi*-LAT paper on dwarf spheroidals (134) (solid black), on the isotropic diffuse (162) (dotted), on the Galactic center halo for an NFW profile (172) (dashed). The yellow (95%) and green (68%) bands give the range of expected limits when repeating the procedure multiple times in Monte-Carlo simulations on dwarf spheroidals without the inclusion of a signal. The light green (Einasto) and light gray (NFW) band give the expected CTA sensitivity (500 hours) for the Galactic center halo under the assumption of two different dark matter profiles. For these CTA estimates, the contribution by the US groups (doubling the number of mid-sized telescopes) was taken into account. For the Einasto halo model the shape parameter was fixed to 0.17. For both models the density was normalized to 0.4 GeV cm^{-3} at the solar radius. For the sensitivity curves, the signal was evaluated by integrating the product of the gamma-ray acceptance and the differential DM flux over an annulus of $0.3 - 1.0$ deg from the GC. The background in the signal region was calculated from the product of the signal region solid angle and an energy-dependent model for the spatial density of protons and electrons that survive background rejection cuts. In addition, the uncertainty on the background was modeled by assuming the existence of a control region with a solid angle five times that of the signal region.

near future the community is looking toward the next generation ground-based instrument as the next big step in gamma-ray astrophysics¹. The Cherenkov Telescope Array (CTA) is expected to start operation in 2017 with a partially completed array (current start of construction planned for 2016). It will provide sensitive observations of the gamma-ray sky over the energy range from a few tens of GeV to 100s of TeV. To achieve the optimal sensitivity over that wide a range in energy, CTA will employ three different telescope sizes: Large Size Telescope (LST, 23 m diameter), Medium Size Telescope (MST, 10-12 m) and Small Size Telescope (SST, 4-6 m). The design goal is a point-source sensitivity of at least

¹it should be noted, that the planned Russian/Italian space-mission *Gamma-400* (173) aims to significantly improve the angular and energy resolution which might be relevant for line searches

an order of magnitude better than currently operating instrument at the sweet-spot of 1 TeV and a significantly improved angular resolution, improving with energy from 0.1° at 100 GeV to better than 0.03° at energies above 1 TeV (174).

Even though *Fermi*-LAT has now unambiguously demonstrated that protons are accelerated in the shock waves of SNRs, many questions about the origin of CRs remain open: the maximum energy imparted on particles in shock waves, the magnification of the ambient magnetic field to achieve those high energies, the overall efficiency of converting explosion energy into the acceleration of particles. CTA with its enhanced sensitivity and angular resolution will add valuable information to this puzzle. The HAWC detector is about to be completed and will survey the sky continuously at the highest gamma-ray energies (around 10–100 TeV) with particular sensitivity to hard spectrum extended sources. Additionally, neutrino detectors, such as IceCube (175) are now starting to detect astrophysical neutrinos (176) at very high energies above ~ 100 TeV. While the current data set is consistent with a diffuse isotropic flux of neutrinos, pinpointing individual sources will significantly improve our understanding of CR acceleration at the highest energies and should be possible with the next-generation in-ice or mediteranean detector (177).

Gamma rays are sensitive to almost any annihilation channel with a sensitivity that is closely related to the total annihilation cross section of dark matter that underlies its total relic abundance today. Already now, gamma-ray limits are probing below the thermal relic interaction rate for some of the preferred WIMP mass range. While direct detection experiments mostly have to deal with uncertainties in the background estimations, the indirect detection technique is largely dominated by astrophysical uncertainties. For dwarf spheroidal galaxies, these are largely mitigated by the lack of astrophysical backgrounds and tight constrains on the halo profile from dynamical measurements. For the Galactic center these uncertainties are the largest but the prospects for a detection are still the highest. A positive (and credible) detection would entail either a gamma-ray line, as in the case of the aforementioned one at 130 GeV in the *Fermi*-LAT data or alternatively, from the measurement of identical spectra that are compatible with a dark matter origin from more than one source. None of the proposed dark matter search methods (direct detection, indirect detection or accelerator searches) will be able to unambiguously claim the detection of dark matter and thus all the methods are crucial in a viable dark matter program for the future. Each potential signal will potentially be created by a new (previously unknown) background – even in the case of accelerator searches. One big advantage of the indirect detection techniques is that if a signal is found in an accelerator or in a direct detector, gamma-ray measurements will provide the only way to connect the laboratory to the actual distribution of dark matter on the sky and identify the nature of the particle through the details of the annihilation process. In fact detecting a signal from the Galactic center would allow to measure the dark matter density profile and feed back to cosmological simulations. In addition, there is a unique region of the WIMP parameter space that CTA can best address in the near future – the high-mass (~ 1 TeV) scenario (178).

The field still has lots of open question that we would like to answer in the future. Where are the Pevatrons? What is the CR content in supernova remnants or in Galaxy clusters? Up to what energies do GRBs accelerate particles? Can giant pair halos around AGNs be detected? What is the particle nature of dark matter, is the WIMP scenario valid and if yes, what is the mass and annihilation cross section of this particle? Clearly for many of these questions the scientific output from the community would be enhanced if the mission of the *Fermi*-LAT was further extended to provide overlap with HAWC and

with CTA to cover sources over as broad an energy range as possible.

SUMMARY POINTS

1. Gamma-ray observations both from space and from the ground provide an unprecedented detail of the high-energy Universe.
2. While the *Fermi*-LAT has demonstrated the acceleration of protons in SNRs, the hunt for the origin of Galactic CRs (meaning the dominant source of CRs and the acceleration up to 10^{15} eV is still not finally resolved.
3. Young SNRs provide the best candidates for acceleration up to the knee.
4. Indirect searches for dark matter using gamma rays complement and enhance accelerator and direct search efforts.

DISCLOSURE STATEMENT

The authors are not aware of any affiliations, memberships, funding, or financial holdings that might be perceived as affecting the objectivity of this review.

ACKNOWLEDGMENTS

I would like to thank everyone who was involved in the preparation of this manuscript, including Elliott Bloom, Roger Blandford, Seth Digel, Manuel Kraus, Luigi Tibaldo, David Thompson, and Matthew Wood. Also the support of the anonymous referee is gratefully acknowledged.

7. Supplemental Material

7.1. Use case: the Galactic Center region

The Galactic center is arguably one of the most interesting regions on the gamma-ray sky. When viewed in radio (see e.g. 179), the central few 100 pc of the Milky way shows a complex and very active region, suggesting particle acceleration to very high energies. It is expected to harbor a large number of potential gamma-ray emitters both in the GeV and TeV region. A large population of millisecond pulsars, radio pulsars and SNRs is known to be located within the inner parsec of our Galaxy (180). The density of gas and radiation fields for the interaction of CR protons and electrons in this inner region is large. The very center of our Galaxy can be expected to accelerate particles to relativistic energies either through a hypothetical termination shock of a wind from the supermassive black hole (see e.g. 181) or the combined effect from stellar wind shocks (182), thereby additionally contributing to the gamma-ray flux from the region. On top of all these astrophysical particle accelerators the Galactic center region is expected to be the brightest source of dark matter annihilation gamma rays on the sky by at least two orders of magnitude.

In the following I will focus on the inner 5° from the Galactic center and describe the observational data and the conclusions that can be drawn from the observations of that region. An observational overview of the region is given in Figure 11 and Figure 12.

7.1.1. The Central gamma-ray source. The most prominent source of gamma rays across all energy bands in this region is coinciding with the kinematic center of the Galaxy and the strong compact radio source Sgr A*, the location of the $4.3 \times 10^6 M_\odot$ supermassive black hole. The gamma-ray source was detected at TeV energies (HESS J1745–290) by several IACTs in the early 2000s (183, 184, 185) and also at GeV energies (186, 187, 59, 188) – dubbed 3FGL J1745.6–2859c. The spectral shape of the GeV–TeV emission does not favor a dominant dark matter annihilation scenario (see Figure 12 and (188, 189)), although (190) and (191) recently suggested a combination of a powerlaw and a heavy dark matter annihilation spectrum) and an association with an astrophysical particle accelerator seems more likely. Detailed studies of the position of the source with the high-angular resolution of H.E.S.S. has provided the most accurate position to date (192): the source is within $8'' \pm 9''_{stat} \pm 9''_{sys}$ from the position of Sgr A* with an upper limit on the extension of the source of $1.3'$ (95% confidence level). This measurement rules out the SNR Sgr A East as a source of the gamma-ray emission, leaving two main objects as possible astrophysical counterparts: the supermassive black hole Sgr A* or the pulsar wind nebula PWN G359.95–0.04 (193). PWNe are known to accelerate particles (mostly e^- and e^+) to beyond TeV energies (see e.g. the Crab Nebula) and a scenario for the H.E.S.S. spectrum was presented by (194). The supermassive black hole itself might also accelerate particles (195) and the gamma-ray emission could originate within an $O(10)$ pc zone due to interaction of runaway protons with the ambient medium (196, 197) or by electrons accelerated in termination shocks driven by strong winds from the black hole (181). With the addition of the *Fermi*-LAT data to lower energies (188) the spectral shape seems to rule out a single-source leptonic scenario from G359.95–0.04 and emission related to Sgr A* seems the most likely explanation. A single hadronic scenario for the emission is still possible, although the diffusion coefficient derived from the point-like nature of the emission is rather small. Various authors have employed more complex hybrid or flaring scenarios (188, 198, 199) that can explain the gamma-ray spectral and morphological properties. In the future CTA observations might further

improve the localisation accuracy of the gamma-ray source. In addition, a compelling way to relate the emission to the black hole has recently been proposed by (200). The passage of early-type or giant stars approaching the line of sight will induce pair-production eclipses that will produce a characteristic time- and energy-dependence in the gamma-ray emission in the 100–300 GeV band. The projected dimming by a few percent for a few weeks should be detectable with an instrument such as CTA and would locate the size of the VHE emitting region to the inner 1000 Schwarzschild radii.

7.1.2. The Galactic Center ridge. Moving further out, H.E.S.S. has reported the detection of diffuse gamma-ray emission from the Galactic center ridge that is well correlated with molecular clouds in the central 200 pc of the Milky way and is confined to the region $|l| < 0.8^\circ$, $|b| < 0.3^\circ$ (201). The close correlation with the interstellar material and the spectral shape (photon index of $\Gamma = 2.3$) of the emission suggested a hadronic origin in which what is observed is the result of CRs diffusing from the region. The spectrum is harder than the spectrum of the Galactic disk and the flux above 1 TeV is about a factor of 3-9 times higher than that in the Galactic disk. This led the authors to argue for an additional population of CRs in the inner 200 pc of the Milky way, possibly produced by a combination of several SNRs (201). Recently, (202) showed that the GeV (*Fermi-LAT*) gamma-ray emission in this region is well correlated with the extended morphology observed at radio, X-ray and TeV energies and can be described with a broken power law spectral model with $\Gamma_1 = 1.8$, $\Gamma_2 = 3.0$, and $E_{\text{break}} = 2.5\text{GeV}$. These authors suggested a non-thermal bremsstrahlung origin of the broad-band emission from two populations of electrons (one cooled population responsible for the radio and GeV emission, the other uncooled population responsible for the TeV emission), although the magnetic field required for this interpretation is surprisingly low – $O(10 \mu\text{G})$. Also (203) concluded that a GeV component coincident with the H.E.S.S.-detected TeV Galactic ridge emission is present and that its morphology matches the 20-cm radio emission. Other hybrid models that employ a combination of hadronic and leptonic processes to describe the gamma-ray emission in the ridge are e.g. given in (204)

7.1.3. The Fermi-LAT Galactic Center Excess. The most tantalising hint for new physics has been detected in the form of an extended radially symmetric excess in the very center of our Galaxy. After the original claim by (209), many studies have confirmed the basic properties (207, 210, 211, 203, 212, 213), although the stability of these properties with respect to changes in the assumptions about the Galactic diffuse foreground model is still an open issue. It should be noted that the signal comprises about 10% of the total emission in the inner Galaxy when integrated in the appropriate region. Nevertheless, many of the alleged properties of the signal seem to be consistent with a dark matter annihilation origin for a particle of mass 10–40 GeV for a radially symmetric dark matter profile following $\rho_{DM} \propto r^{-\gamma}$ with r being the radial distance to the Galactic center and γ in the range 1.1 to 1.3 (214). The velocity-averaged annihilation cross-section needed to explain the emission with a dark matter origin comes out to a reasonable $\sigma_v = 1.6 \times 10^{-26} \text{ cm}^3/\text{s}$. The signal seems to be radially symmetric and is extended out to rather large radii ($r \sim 10^\circ$, corresponding to $\sim 1.5 \text{ kpc}$). It should, however, be noted, that also astrophysical sources might be responsible for the emission, most notably CRs injected in the Galactic center (215, 216) or a population of unresolved point sources such as milisecond pulsars (MSPs) (212, 217, 218, 219, 220, 221, 222, 223). MSPs show a similar spectrum, peaking at

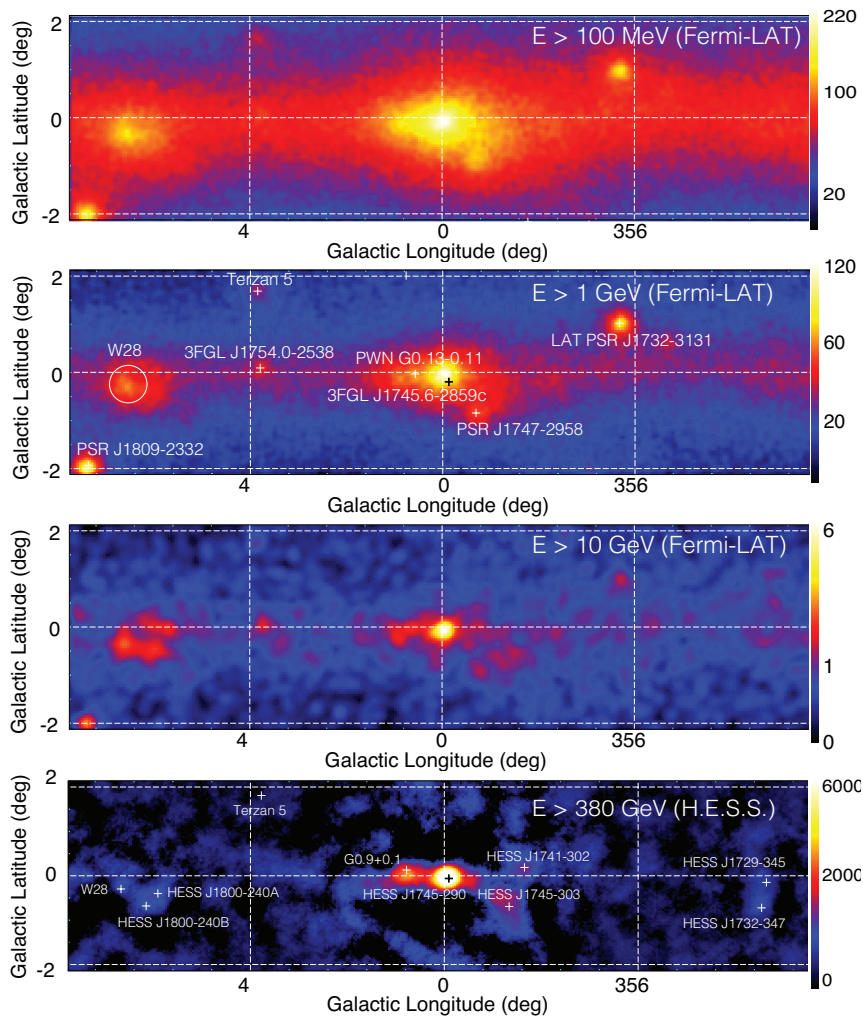


Figure 11

Region around the GC ($|l| < 8^\circ$, $|b| < 2^\circ$) in gamma rays for different minimum energies. The region corresponds to a size of 1100×280 pc. The top three panels are smoothed gamma-ray count maps (top two: Gaussian of width 0.1° , third: Gaussian of width 0.2°) as observed with the *Fermi*-LAT for the ultraclean class and 6.5 years of data (August 2008 – February 2015). The pixel size is 0.05° , the z-scale shows counts per pixel in a square root scaling. Several prominent sources from 3FGL catalog are marked in the second panel illustrating the variety of sources. It should be noted that a significant number of sources from 3 FGL were not marked in this panel. The fourth panel shows a H.E.S.S. excess map from the Galactic plane survey as published for the 2004 data in (58) for hard cuts above 380 GeV. The TeV-detected sources from TeVCat webpage (<http://tevcat.uchicago.edu>) are marked, although it should be stressed that only 1 year of data was used in the map and certain areas of this region received a significantly larger amount of observations in subsequent years.

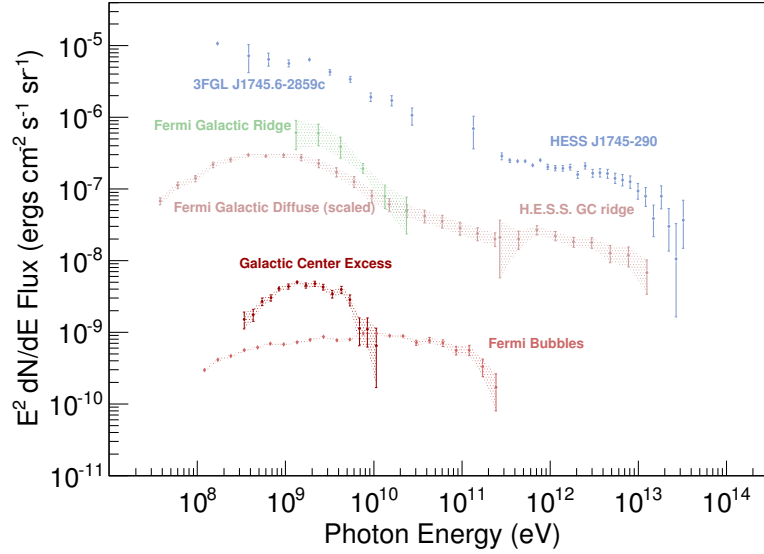


Figure 12

Spectral energy distribution for the gamma-ray sources found in the inner Galaxy. The most prominent source is the central source, coinciding with Sgr A* (3FGL J1745.6–2859c, HESS J1745–290) shown in light blue (205, 188). Next in terms of surface brightness is the Galactic center ridge emission (light red) that has also been observed at GeV energies (green). Also shown for comparison is the *Fermi*-LAT Galactic diffuse emission measured in the region $|l| < 80^\circ$, $|b| < 8^\circ$ (labeled *Fermi Galactic Diffuse (scaled)*). This emission has been scaled up by a factor of 5. The factor of 5 is a combination of a factor of 15 difference in average column densities of neutral interstellar gas integrated over the line of sight (assuming $X_{CO} = 0.5 \times 10^{20}$ molecules cm^{-2} $(\text{K km/s})^{-1}$ for the inner region and $X_{CO} = 1.5 \times 10^{20}$ molecules cm^{-2} $(\text{K km/s})^{-1}$ in the larger region and furthermore assuming an HI spin temperature of 150 K, and a dust-to-gas ratio of $73 \times 10^{20} \text{ cm}^{-2} \text{ mag}^{-1}$ to correct for dark gas) and the hadronic emission related to the gas being about 30% of the total emission in the larger region (206), resulting in an overall factor of 5. Also shown is the *Fermi*-LAT detected Galactic Center Excess (dark red) taken from (207) and the emission from the Fermi-Bubbles (208) fitted in a much larger region. It should be noted, that in a consistent analysis, all components would have to be fitted simultaneously (along with all the other point and extended sources in the region), while some of the publications referred to in the text have done this, not all of the publications from which the spectral data points are taken have done this for the Galactic center region.

$\sim 1 - 3\text{GeV}$ and their spatial distribution might match the excess signal (as suggested by the spatial distribution of low-mass X-ray binaries (224, 211). Determining the properties of the unresolved population of MSPs relies heavily on *Fermi*-LAT data itself (derived from the ~ 60 detected MS pulsars) which might already constitute a biased sample and might not be representative for the MSP population in the very center of the Galaxy. As noted by (225), DM annihilation would release energy in annihilation products at a rate of $\sim 3 \times 10^{37}$ erg/s within the innermost 150 pc of the Galaxy compared to 10^{39} erg/s injected in accelerated hadrons and 10^{38} erg/s in accelerated leptons from star-formation (SNRs, stellar winds). Energetically, a scenario in which the emission is related to CR protons or electrons is therefore completely reasonable (215, 216).

7.1.4. The Fermi-LAT Galactic Center Line emission. A lot of excitement also revolved around the alleged detection of a gamma-ray line feature at 130 GeV in the Galactic center data of the *Fermi*-LAT (226). While the original publication claimed a post-trial significance of 3.2σ that was later confirmed by others (227, 228), the time-evolution of the signal did not increase as expected for a real signal. Furthermore, an analysis with updated instrument response functions (*Pass 7 reprocessed*) further dropped the significance of this signal, so that at this point the data points towards a statistical fluctuation rather than a real signal (229).

7.1.5. The Fermi Bubbles. Possibly the most surprising discovery in all of high-energy astrophysics in recent years has been the discovery of the *Fermi bubbles*, large scale structures that extend up to 11 kpc above and below the Milky way galaxy. The spectrum of these structures is hard $\sim E^{-1.9\pm 0.2}$ with an exponential cut off at high energies at 110 ± 50 GeV and also rolling over below 1 GeV. The emission is rather uniform in intensity across the bubbles (with an enhancement in the south-east) and the spectrum does not change throughout the bubbles. The edges are rather sharp ($\sim 3.5^\circ$). The bubble spectral shape matches both a leptonic and a hadronic scenario, although if the WMAP haze is taken into account the leptonic scenario fits all available data with less assumptions (see e.g. 230). Given their position on the Galactic center, the bubbles seem to originate from that region (also evidenced by the tighter waist in the Galactic plane). An obvious candidate is activity in the recent past (< 1 Myr) of the SMBH - which could easily supply the energy required to blow the bubbles ($\sim 10^{56}$ erg). Other scenarios include nuclear star-formation in the Galactic center region that could in principle inflates the bubbles if the hot gas, CRs and magnetic fields can be integrated over sufficiently long timescales (231, 110). Other explanations include a jet from the black hole (232, 233, 234, 235), a spherical outflow from the black hole (236) or a sequence of shocks from several accretion events onto the black hole (105).

What should be clear from the description in this section is that the Galactic center region is highly complex and complicated with a large number of not-yet-understood astrophysical acceleration and diffusion phenomena. The situation is further complicated by the presence of a highly structured and extremely bright diffuse gamma-ray background arising from the interaction of the pool of CRs with dense material in the inner Galaxy. The whole region is our closest test-bed to study these phenomena. On top of it, there is the exciting possibility of new physics (dark matter annihilation) in this region – however, before a signal can be claimed, all other astrophysical phenomena have to be understood to a level where they can be ruled out to contribute to the alleged dark matter signal.

7.2. High-energy charged particles in space

7.2.1. Particle acceleration. The two main mechanisms that can accelerate particles in astrophysical environments are: static electric fields or head-on collisions with magnetic turbulences. The acceleration in electric fields is readily understood, however, in astrophysical systems special conditions are necessary to achieve a large-scale electric field due to the high conductivity of astrophysical plasmas (the electric fields are short-circuited by the motion of the free charges). Examples for astrophysical systems in which large-scale electric fields play a role are *unipolar inductors* (rotating black holes or neutron stars) or systems with *magnetic reconnection* (where locally regions with opposite orientations of the

magnetic field merge).

The second probably more common acceleration mechanism happens in astrophysical shocks – where two fluids are compressed by the compression ratio r . In shocks *Fermi processes* (head-on collisions of particles with magnetic turbulences) can accelerate particles (for a recent review of shock acceleration see e.g. 21).

Fermi’s original idea was to propose a mechanism in a setting in which (random) collisions with magnetic mirrors between charged particles and interstellar clouds could result in the acceleration of particles (237). In the original proposal in which clouds with random propagation directions were the agents of collisions, the process was relatively slow and inefficient. Energy-increasing approaching and energy-decreasing receding collisions were cancelling each other out and therefore the energy gains per collision were only second order in the ratio of cloud velocity u to particle speed v , or $\Delta E/E \sim (u/v)^2$. In the late 1970s several researchers (238, 239, 240, 241) realised independently that in strong shocks a reference frame existed in which the fluids before and behind the shocks always converged – and therefore only approaching (head-on) collisions which increased the energy of the particle were happening. These processes were shown to allow for energy gains of first order in u/v , or $\Delta E/E \sim u/v$, with every shock crossing and therefore a much more rapid acceleration. An important prediction of the theory is that the accelerated particles exhibit a number spectrum in momentum space (in the test particle limit in which the accelerated particles are energetically unimportant) following $N(p) \sim p^{-3r/(r-1)}$. For strong shocks $r = 4$ and therefore $N(p) \sim p^{-4}$ or $N(E) \sim E^{-2}$.

The second important property of the acceleration process is the maximum energy the particles can reach. For this property the balance between energy gain and energy losses during the acceleration become relevant. Very generally energy can be lost if the particle escapes from the shock region (if the gyro-radius of the particle exceeds the shock size), or if the energy losses of the particles become larger than the energy gains per shock crossing. These processes lead to an energy spectrum of the accelerated particles that resembles a powerlaw in energy with an exponential cutoff above some energy E_{\max} (242, 243). In general an expression for E_{\max} can be found by equating the acceleration time in the shock to the lesser of the radiative loss time or the escape time. As shown by (21) the typical maximum energy achievable is:

$$E_{\max,\text{age}} \sim 0.5u_8^2 t_3 B_{\mu G} \quad \text{TeV} \quad (5)$$

$$E_{\max,\text{loss}} \sim 100u_8 B_{\mu G}^{-1/2} \quad \text{TeV} \quad (6)$$

With $u_8 = u/10^8 \text{ cm s}^{-1}$, $t_3 = t/1000 \text{ years}$ and B the upstream magnetic field in μG .

Finally (especially for older systems), if escape of particles from the acceleration region is the limiting factor, the maximum energy should behave as.

$$E_{\max}(\text{escape}) \sim 10B_{\mu G} \lambda_{17} \quad \text{TeV} \quad (7)$$

with $\lambda_{17} = \lambda_{\max}/10^{17} \text{ cm}$.

For typical timescales and shock speeds (t_3 , and u_8 of order 1), these are energies accessible by ground-based arrays of gamma-ray telescopes.

It can be shown, that for any energetically possible source of CRs, a substantial amount of energy must be contained in the accelerated particles. Those particles will have a dynamical (non-linear) effect on the shock which means that the test-particle limit will no

longer be applicable (244). Most importantly, the pressure of the accelerated particles will slow down the incoming fluid (in the shock frame) by diffusing ahead. These non-linear effects will therefore decrease the compression ratio close to the shock (and thereby make the spectrum softer i.e. Γ larger) but increase the compression ratio far ahead of the shock (and thereby make the spectrum harder i.e. Γ smaller). The resulting overall particle spectrum would deviate from the traditional $\Gamma = 2$ case both at low energies (where the spectrum would be softer) and at high energies (where the spectrum would be harder). A clear test of the theory and the non-linear effects described here would be a concave spectrum of the accelerated particles (note that this effect is most relevant for protons).

7.2.2. Particle Propagation. One of the fundamental assumption about the shock acceleration processes is that particles move diffusively through space with $\langle r^2 \rangle = 2Dt$ (with D the Diffusion coefficient). D governs the speed of the diffusion process and depends on both the average magnetic field B and its turbulence δB (on length-scales comparably to the gyroradius R_g). In the Bohm limit – the slowest possible diffusion – particles diffuse perpendicular to magnetic field lines. The mean free path of the particles is thus given by the gyroradius and the resulting diffusion coefficient can be estimated as $D \sim \eta R_g c/3$ with $\eta \approx (\delta B/B)^2$ (245). The gyroradius for particles of unit charge can be written as $R_{g,pc} \approx 0.001 E_{\text{TeV}}/B_{\perp,\mu G}$ and therefore following (18):

$$\langle r_{pc}^2 \rangle^{1/2} \approx 0.01 (\eta E_{\text{TeV}} t_{yr} / B_{\perp,\mu G}) \quad (8)$$

When describing the diffusion of particles in our Galaxy as a whole one typically comes to the conclusion that the diffusion coefficient is of the form $D = 10^{28} (E/10\text{GeV})^\delta \text{cm}^2 \text{s}^{-1}$ with $\delta = 0.3 - 0.7$ (246). This energy dependence can be assumed to be spatially varying and should reflect the local distribution of magnetic turbulence.

7.2.3. Energy losses. Energetic particles lose energy via various processes which invariably leads to the generation of photons all across the electromagnetic spectrum from radio to high-energy gamma rays. In the gamma-ray energy band, there are various competing processes that can be used to explain the observed gamma-ray emission. The main radiation and energy loss mechanisms all involve the interaction of high-energy charged particles with magnetic fields (synchrotron emission of both electrons and protons), photon fields (inverse Compton scattering of electrons or photo-meson production from protons) or matter (bremsstrahlung, p-p collisions).

Electron cooling times. Unless in very dense radiation fields electrons in typical Galactic environments above energies of $\sim 1\text{GeV}$ lose energy mainly through synchrotron radiation or (at low magnetic fields) through inverse Compton scattering. Given the ubiquity of the cosmic microwave background (CMB), as well as other photon fields in the Universe, inverse Compton scattering is present with high efficiency over the whole gamma-ray band. In the Thomson regime inverse Compton cooling decreases linearly with energy and therefore this process is particularly important at very high electron energies.

The expression for the Inverse Compton scattering cooling time is (45):

$$\tau_{\text{IC}} = 4 \times 10^8 f_{KN}^{-1} \left(\frac{U_R}{1\text{eVcm}^{-3}} \right)^{-1} \left(\frac{E_e}{\text{GeV}} \right)^{-1} \text{yr} \quad (9)$$

Where U_R is the radiation density of the photon fields and E_e is the electron energy.

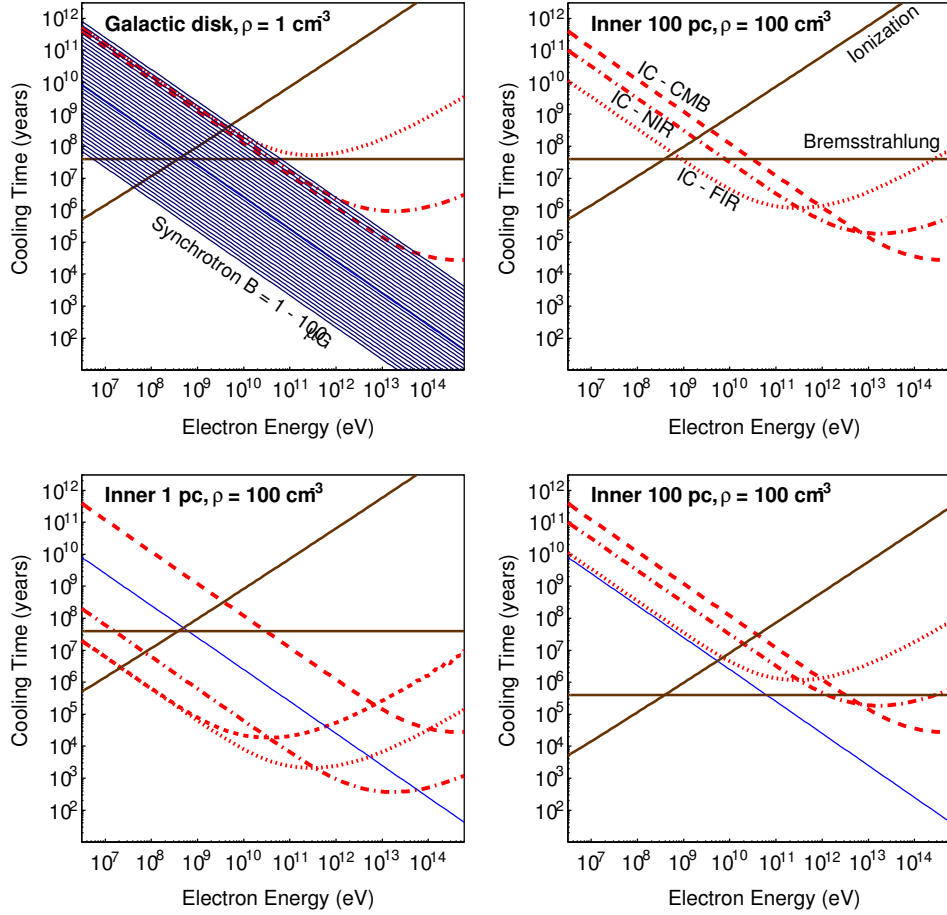


Figure 13

Cooling time scales for relativistic electrons for various processes in typical Galactic environment. For all plots the energy density of the CMB is $U_{\text{CMB}}(kT = 2.35 \times 10^{-4} \text{eV}) = 0.26 \text{eVcm}^{-3}$, the matter density is $n_0 = 1 \text{cm}^{-3}$ unless for the bottom right plot where $n_0 = 100 \text{cm}^{-3}$: (Top left): radiation fields in a typical Galactic environment $U_{\text{NIR}}(0.3 \text{eV}) = 0.2 \text{eVcm}^{-3}$, $U_{\text{FIR}}(6 \times 10^{-3} \text{eV}) = 0.2 \text{eVcm}^{-3}$. (Top right): radiation fields in the Galactic disk in the inner 100 pc from the Galactic center ($U_{\text{NIR}}(0.3 \text{eV}) = 9 \text{eVcm}^{-3}$, $U_{\text{FIR}}(6 \times 10^{-3} \text{eV}) = 1 \text{eVcm}^{-3}$). (Bottom left): radiation fields in the inner 1pc^3 from the Galactic center ($U_{\text{Opt}}(3 \text{eV}) = 5000 \text{eVcm}^{-3}$, $U_{\text{NIR}}(0.3 \text{eV}) = 5000 \text{eVcm}^{-3}$, $U_{\text{FIR}}(6 \times 10^{-3} \text{eV}) = 5000 \text{eVcm}^{-3}$). Bottom right: like top right (inner 100 pc) with a matter density of $n_0 = 100 \text{cm}^{-3}$.

In the Thomson regime the loss rate $dE/dt (= E_e/\tau)$ is therefore proportional to E^2 and therefore Inverse Compton scattering depletes the high-energy part of the electron spectrum stronger than the low-energy part (resulting in a steeper electron spectrum dN/dE). For highly energetic electrons the classical electron cross section gets reduced through relativistic effects (*Klein-Nishina* or KN formula) essentially due to energy conservation between the up scattered photon and the incident electron. The corresponding increase in loss time can

be parameterised (247) by the factor $f_{KN} \approx (1 + b)^{-1.5} = (1 + 40E_{e,\text{TeV}}kT_{\text{eV}})^{-1.5}$. This factor is approximately equal to 1 for small energies (Thomson regime) and proportional to $\ln(E_e)/E_e^2$ for very large energies with a transition regime in between. Thus in the deep KN regime $\tau_C \propto E_e/\ln(E_e)$ and therefore the electron spectrum becomes harder with IC losses. It is interesting to note, that in the Thomson regime the cooling time does not depend on the spectrum of target photons but only on the total radiation density. This is not true for the Klein-Nishina regime. The expression for synchrotron cooling is very similar to the above expression for Inverse Compton scattering when one replaces U_r with $U_B = B^2/(8\pi)$:

$$\tau_{\text{Synch}} = 2.5 \times 10^9 \left(\frac{B}{1\mu\text{G}} \right)^{-2} \left(\frac{E_e}{\text{GeV}} \right)^{-1} \text{ yr} \quad (10)$$

The cooling time for electrons due to Bremsstrahlung is energy-independent and depends only on the density of hydrogen atoms n_0 :

$$\tau_{\text{Br}} = 4 \times 10^7 \left(\frac{n_0}{1\text{cm}^{-3}} \right)^{-1} \text{ yr} \quad (11)$$

The density and location of the interstellar material (mostly consisting of molecular clouds, HI, and H₂ regions) can be measured using radio, microwave and optical observations (248). Because the cooling time is energy-independent Bremsstrahlung does not change the initial electron energy spectrum - even further, the bremsstrahlung gamma-ray spectrum simply repeats the parent electron spectrum. In hydrogen gas below ~ 350 MeV ionisation losses dominate over Bremsstrahlung. The corresponding cooling time is (249):

$$\tau_{\text{Io}} = 4.1 \times 10^9 \left(\frac{E_e}{\text{GeV}} \right) \left((3 * \ln(E_e/\text{GeV}) + 42.5) \frac{n_0}{1\text{cm}^{-3}} \right)^{-1} \text{ yr} \quad (12)$$

The electron loss processes are illustrated in Figure 14 for different Galactic environments (top left: Galactic disk, top right: inner 100 pc in the Galactic disk with respect to the Galactic Center, bottom left: inner 1 pc of the Galaxy, bottom right: like top right but with a significantly higher matter density). As can be seen, at high energies and high magnetic fields synchrotron emission is the dominant loss process of relativistic electrons.

Proton cooling times. The main cooling mechanism for relativistic protons below 10^{15} eV in a hydrogen (target) medium is the inelastic scattering resulting in the production of secondary pions (π), eta (η), kaons and hyperons. While nearly 100% of neutral pions (π^0 s) decay into two photons, the branching ratio of $\eta \rightarrow \gamma\gamma$ is only 40%. Similar to the case of Bremsstrahlung the cooling time above proton energies of $E_p = 1\text{GeV}$ is almost independent of energy (a result of the fact that the total pp scattering cross section σ_{pp} is almost energy-independent), The cooling time can be given as:

$$\tau_{\text{pp}} = (n_0)^{-1} (\sigma_{\text{pp}} f c)^{-1} = 5.3 \times 10^7 \left(\frac{n_0}{1\text{cm}^{-3}} \right)^{-1} \text{ yr} \quad (13)$$

therefore the initial (acceleration) energy spectrum of the protons remains unaffected. At higher proton energies and extragalactic environments with low hydrogen densities proton synchrotron and photo-pion production becomes important.

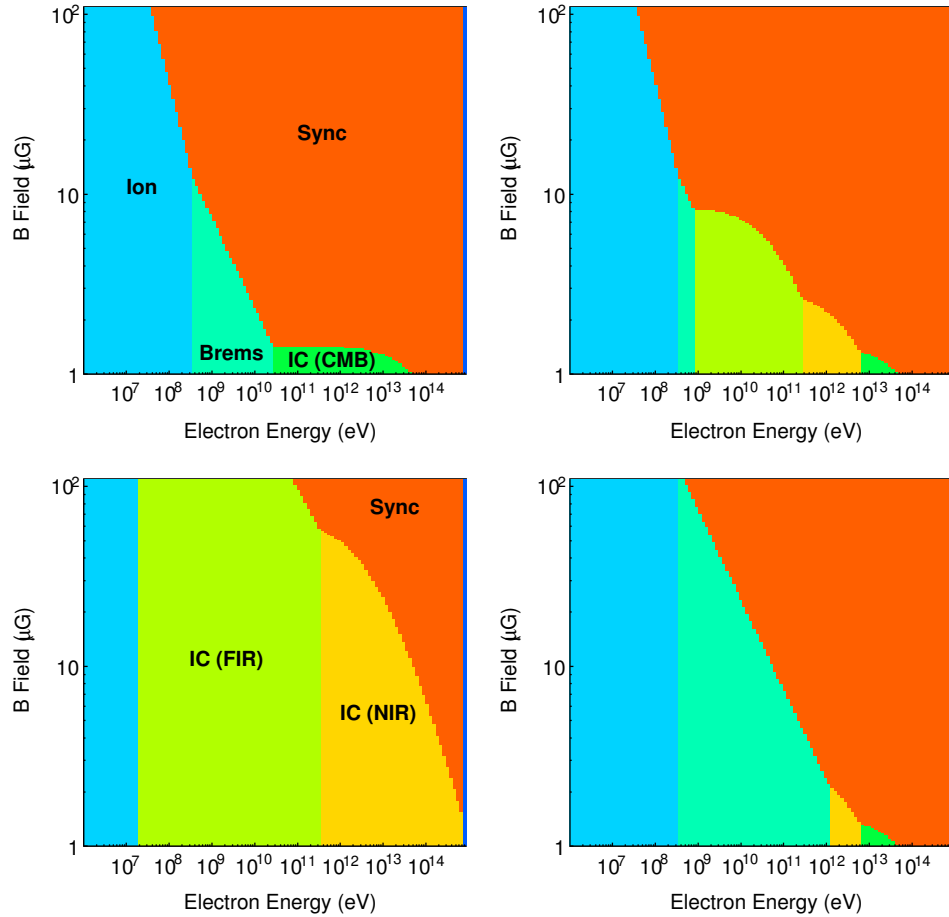


Figure 14

Dominant loss processes (i.e. the process with the minimum cooling time) for the radiation fields and densities used in Figure 13 as a function of magnetic field and as a function of energy. In the blue region ionization dominates, in the red region synchrotron emission, light green corresponds to Bremsstrahlung, and green and orange to the various Inverse Compton components.

LITERATURE CITED

1. Aharonian F, et al. *Astron. Astrophys.* 464:235 (2007)
2. Atwood WB, et al. *ApJ* 697:1071 (2009)
3. Tavani M, et al. *A&A* 502:995 (2009)
4. Vincent P. 2005. In *International Cosmic Ray Conference*, vol. 5 of *International Cosmic Ray Conference*
5. Sitarek J, et al. *ArXiv e-prints* (2013)
6. Kieda DJ. *ArXiv e-prints* 1308.4849 (2013)
7. Morrison P. *Il Nuovo Cimento* 7:858 (1958)
8. Kraushaar WL, Clark GW. *Phys. Rev. Lett.* 8:106 (1962)
9. Klebesadel RW, Strong IB, Olson RA. *ApJ* 182:L85 (1973)

10. Kraushaar WL, et al. *ApJ* 177:341 (1972)
11. Fichtel CE, et al. *ApJ* 198:163 (1975)
12. Bignami GF, et al. *Space Science Instrumentation* 1:245 (1975)
13. Hartman RC, et al. *ApJS* 123:79 (1999)
14. Galbraith W, Jelley JV. *Nature* 171:349 (1953)
15. Jelley JV, Porter NA. *Quarterly Journal of the Royal Astronomical Society. Vol. 4* 4:275 (1963)
16. Weekes TC, et al. *Astrophys. J.* 342:379 (1989)
17. Daum A, et al. *Astroparticle Physics* 8:1 (1997)
18. Hinton JA, Hofmann W. *Annual Review of Astronomy & Astrophysics* 47:523 (2009)
19. Dermer CD (2013). Sources of GeV Photons and the Fermi Results. Aharonian, F. and Bergström, L. and Dermer, C., 225
20. Caraveo PA. *Annual Review of Astronomy & Astrophysics* 52:211 (2014)
21. Reynolds SP. *Annual Review of Astronomy & Astrophysics* 46:89 (2008)
22. Bergström L. *Annalen der Physik* 524:479 (2012)
23. Conrad J. *ArXiv e-prints, 1411.1925* (2014)
24. Funk S. *Proceedings of the National Academy of Sciences* (2014)
25. Bertone G, Hooper D, Silk J. *Phys. Rep.* 405:279 (2005)
26. Bykov A, et al. *Space Sci. Rev.* 173:309 (2012)
27. Rieger FM, de Oña-Wilhelmi E, Aharonian FA. *Frontiers of Physics* 8:714 (2013)
28. Bergström L, Snellman H. *Phys. Rev. D* 37:3737 (1988)
29. Amelino-Camelia G, et al. *Nature* 393:763 (1998)
30. Steigman G, Turner MS. *Nuclear Physics B* 253:375 (1985)
31. Feng JL. *ARA&A* 48:495 (2010)
32. Ellis J, et al. *Nuclear Physics B* 238:453 (1984)
33. Hooper D, Profumo S. *Phys. Rep.* 453:29 (2007)
34. Baltz EA, et al. *JCAP* 7:13 (2008)
35. Porter TA, Johnson RP, Graham PW. *ARA&A* 49:155 (2011)
36. Ellis J, Hagelin JS, Nanopoulos DV, Srednicki M. *Nuclear Physics B* 241:381 (1984)
37. Albert J, et al. *ApJ* 669:862 (2007)
38. Aharonian F, et al. *Physical Review Letters* 101:170402 (2008)
39. Abdo AA, et al. *Nature* 462:331 (2009)
40. Madau P, Phinney ES. *ApJ* 456:124 (1996)
41. Franceschini A, Rodighiero G, Vaccari M. *A&A* 487:837 (2008)
42. Sánchez-Conde MA, et al. *Phys. Rev. D* 79:123511 (2009)
43. Abramowski A, et al. *Phys. Rev. D* 88:102003 (2013)
44. Aharonian FA, Atoyan AM, Kifune T. *MNRAS* 291:162 (1997)
45. Blumenthal GR, Gould R.J. *Rev. Mod. Phys.* 42:237 (1970)
46. Drury LO, Aharonian FA, Voelk HJ. *Astron. Astrophys.* 287:959 (1994)
47. Gabici S, Aharonian FA, Blasi P. *Ap&SS* 309:365 (2007)
48. Stecker FW. *Ap&SS* 6:377 (1970)
49. Bergström L, Ullio P, Buckley JH. *Astroparticle Physics* 9:137 (1998)
50. Bringmann T, Bergström L, Edsjö J. *Journal of High Energy Physics* 1:49 (2008)
51. Abeyskara AU, et al. *Astroparticle Physics* 50:26 (2013)
52. Funk S, Hinton JA. *Astroparticle Physics* 43:348 (2013)
53. Ackermann M, et al. *ApJS* 203:4 (2012)
54. Selesnick RS, Looper MD, Mewaldt RA, Labrador AW. *Geophysical Research Letters* 34:n/a (2007)
55. Atwood W, et al. *Nucl.Instrum.Meth.* A446:444 (2000)
56. Abdo AA, et al. *Physical Review Letters* 104:101101 (2010)
57. Aharonian F, et al. *Science* 307:1938 (2005)

58. Aharonian F, et al. *Astrophys. J.* 636:777 (2006)
59. Acero F, et al. *ArXiv e-prints* (2015)
60. Bell AR, Lucek SG. *Mon. Not. R. Astron. Soc.* 321:433 (2001)
61. Lucek S, Bell A. *Astrophysics and Space Science* 272:255 (2000)
62. Green DA. *Bulletin of the Astronomical Society of India* 42:47 (2014)
63. Brandt TJ, et al. *ArXiv e-prints* (2013)
64. Fernandez D, et al. *ArXiv e-prints* (2013)
65. Castelletti G, Dubner G, Clarke T, Kassim NE. *A&A* 534:A21 (2011)
66. Troja E, Bocchino F, Reale F. *ApJ* 649:258 (2006)
67. Albert J, et al. *ApJ* 664:L87 (2007)
68. Acero F, et al. *A&A* 505:157 (2009)
69. Hewitt JW, et al. *ArXiv e-prints* (2013)
70. Ackermann M, et al. *Science* 339:807 (2013)
71. Malkov MA, Diamond PH, Sagdeev RZ. *Nature Communications* 2:194 (2011)
72. Blasi P. *A&A Rev.* 21:70 (2013)
73. Gabici S, Aharonian FA, Casanova S. *MNRAS* 396:1629 (2009)
74. Acciari VA, et al. *ApJ* 698:L133 (2009)
75. Torres DF, Rodriguez Marrero AY, de Cea Del Pozo E. *MNRAS* 387:L59 (2008)
76. Abdo AA, et al. *ApJ* 734:28 (2011)
77. Acciari VA, et al. *ApJ* 730:L20 (2011)
78. Giordano F, et al. *ApJ* 744:L2 (2012)
79. Aharonian F, et al. *Astron. Astrophys.* 370:112 (2001)
80. Humensky TB. 2008. In *American Institute of Physics Conference Series*, ed. F. A. Aharonian, W. Hofmann, & F. Rieger, vol. 1085 of *American Institute of Physics Conference Series*
81. Albert J, et al. *Astron. Astrophys.* 474:937 (2007)
82. Abdo AA, et al. *ApJ* 710:L92 (2010)
83. Yuan Y, et al. *ApJ* 779:117 (2013)
84. Ellison DC, Patnaude DJ, Slane P, Raymond J. *ApJ* 712:287 (2010)
85. Zirkashvili VN, Aharonian FA. *ApJ* 708:965 (2010)
86. Gabici S, Aharonian FA. *MNRAS* 445:L70 (2014)
87. Aharonian F, et al. *ArXiv e-prints* (2014)
88. Morlino G, Caprioli D. *A&A* 538:A81 (2012)
89. Blasi P. *Brazilian Journal of Physics* 44:426 (2014)
90. Grefenstette BW, et al. *ArXiv e-prints* (2015)
91. Aharonian F, et al. *ApJ* 692:1500 (2009)
92. Acero F, et al. *A&A* 516:A62 (2010)
93. Renaud M, et al. 2012. In *American Institute of Physics Conference Series*, eds. FA Aharonian, W Hofmann, FM Rieger, vol. 1505 of *American Institute of Physics Conference Series*
94. Araya M, Frutos F. *MNRAS* 425:2810 (2012)
95. Yuan Q, Huang X, Liu S, Zhang B. *ApJ* 785:L22 (2014)
96. Ackermann M, et al. *Science* 334:1103 (2011)
97. Aharonian F, et al. *A&A* 431:197 (2005)
98. Aliu E, et al. *ApJ* 788:78 (2014)
99. Abdo AA, et al. *ApJ* 658:L33 (2007)
100. Bartoli B, et al. *ApJ* 790:152 (2014)
101. Uchiyama Y, et al. *ApJ* 749:L35 (2012)
102. Hanabata Y, et al. *The Astrophysical Journal* 786:145 (2014)
103. Aharonian F, et al. *A&A* 481:401 (2008)
104. Yang HYK, Ruszkowski M, Zweibel E. *MNRAS* 436:2734 (2013)
105. Cheng KS, et al. *ApJ* 731:L17 (2011)
106. Dogiel VA, Cheng KS, Chernyshov DO, Ko CM. 2014. In *IAU Symposium*, eds. LO Sjouwer-

- man, CC Lang, J Ott, vol. 303 of *IAU Symposium*
107. Chernyshov D. *International Cosmic Ray Conference* 7:11 (2011)
 108. Carretti E, et al. *Nature* 493:66 (2013)
 109. Selig M, Vacca V, Oppermann N, Enßlin TA. *ArXiv e-prints* (2014)
 110. Crocker RM, et al. *ApJ* 791:L20 (2014)
 111. Schure KM, Bell AR. *MNRAS* 435:1174 (2013)
 112. Gabici S, Aharonian FA. *ApJ* 665:L131 (2007)
 113. Blasi P, Amato E, Caprioli D. *MNRAS* 375:1471 (2007)
 114. Bell AR. *MNRAS* 447:2224 (2015)
 115. Abdo AA, et al. *A&A* 512:A7 (2010)
 116. Abdo AA, et al. *A&A* 523:A46 (2010)
 117. Abdo AA, et al. *A&A* 523:L2 (2010)
 118. Abdo AA, et al. *ApJ* 709:L152 (2010)
 119. Ackermann M, et al. *ApJ* 755:164 (2012)
 120. Acero F, et al. *Science* 326:1080 (2009)
 121. Abramowski A, et al. *ApJ* 757:158 (2012)
 122. Acciari VA, et al. *Nature* 462:770 (2009)
 123. Strong AW, et al. *ApJ* 722:L58 (2010)
 124. Lacki BC, et al. *ApJ* 734:107 (2011)
 125. Lacki BC. *MNRAS* 448:L20 (2015)
 126. Flores RA, Primack JR. *Astrophysical Journal* 427:L1 (1994)
 127. Navarro JF, Frenk CS, White SDM. *Astrophysical Journal v.462* 462:563 (1996)
 128. Moore B, et al. *The Astrophysical Journal* 524:L19 (1999)
 129. Jesseit R, Naab T, Burkert A. *The Astrophysical Journal* 571:L89 (2002)
 130. Prada F, et al. *Physical Review Letters* 93:241301 (2004)
 131. Mashchenko S, Wadsley J, Couchman HMP. *Science* 319:174 (2008)
 132. Governato F, et al. *Monthly Notices RAS* 422:1231 (2012)
 133. Catena R, Ullio P. *Journal of Cosmology and Astroparticle Physics* 08:004 (2010)
 134. The Fermi-LAT Collaboration, et al. *ArXiv e-prints* (2013)
 135. Geringer-Sameth A, Koushiappas SM. *Physical Review Letters* 107:241303 (2011)
 136. Kaiser N, et al. *Survey and Other Telescope Technologies and Discoveries. Edited by Tyson* 4836:154 (2002)
 137. The Dark Energy Survey Collaboration. *ArXiv Astrophysics e-prints* (2005)
 138. Ivezić Z, et al. *ArXiv e-prints* (2008)
 139. Tollerud EJ, Bullock JS, Strigari LE, Willman B. *The Astrophysical Journal* 688:277 (2008)
 140. Aliu E, et al. *Physical Review D* 85:62001 (2012)
 141. H. E. S. S. Collaboration, et al. *ArXiv e-prints* (2014)
 142. Albert J, et al. *The Astrophysical Journal* 679:428 (2008)
 143. Pinzke A, Pfrommer C, Bergström L. *Physical Review D* 84:123509 (2011)
 144. Sánchez-Conde MA, et al. *Journal of Cosmology and Astroparticle Physics* 12:011 (2011)
 145. Gao L, et al. *Monthly Notices RAS* 419:1721 (2012)
 146. Dugger L, Jeltama TE, Profumo S. *Journal of Cosmology and Astroparticle Physics* 12:015 (2010)
 147. Huang X, Vertongen G, Weniger C. *Journal of Cosmology and Astroparticle Physics* 01:042 (2012)
 148. Nezri E, et al. *Monthly Notices RAS* 425:477 (2012)
 149. Aleksić J, et al. *Astronomy & Astrophysics* 541:99 (2012)
 150. Arlen T, et al. *The Astrophysical Journal* 757:123 (2012)
 151. Abramowski A, et al. *The Astrophysical Journal* 750:123 (2012)
 152. Ackermann M, et al. *ApJ* 799:86 (2015)
 153. Inoue Y, Ioka K. *Phys. Rev. D* 86:023003 (2012)

154. Murase K, Beacom JF, Takami H. *JCAP* 8:30 (2012)
155. Loeb A, Waxman E. *Nature* 405:156 (2000)
156. Miniati F. *Monthly Notice of the Royal Astronomical Society* 337:199 (2002)
157. Gabici S, Blasi P. *Astroparticle Physics* 19:679 (2003), (c) 2003 Elsevier B.V.
158. Berrington RC, Dermer CD. *The Astrophysical Journal* 594:709 (2003)
159. Pfrommer C, EnBlin TA, Springel V. *Monthly Notices RAS* 385:1211 (2008)
160. Pavlidou V, Fields BD. *The Astrophysical Journal* 575:L5 (2002)
161. Thompson TA, Quataert E, Waxman E. *The Astrophysical Journal* 654:219 (2007)
162. Abdo AA, et al. *Journal of Cosmology and Astroparticle Physics* 04:014 (2010)
163. Abazajian KN, Blanchet S, Harding JP. *Physical Review D* 85:43509 (2012)
164. Bringmann T, Calore F, Mauro MD, Donato F. *Physical Review D* 89:23012 (2014), 2014: American Physical Society
165. Hooper D, et al. *Physical Review D* 86:103003 (2012)
166. Ackermann M, et al. *Physical Review D* 85:83007 (2012)
167. Camera S, Fornasa M, Fornengo N, Regis M. *The Astrophysical Journal Letters* 771:L5 (2013)
168. Behnke E, et al. *Physical Review D* 86:52001 (2012)
169. Aad G, et al. *Journal of High Energy Physics* 04:075 (2013)
170. Chatrchyan S, et al. *Journal of High Energy Physics* 9:94 (2012)
171. Arrenberg S, et al. *eprint arXiv* 1310:8621 (2013), snowmass 2013 CF4 Working Group Report
172. Ackermann M, et al. *The Astrophysical Journal* 761:91 (2012)
173. Galper AM, et al. *ArXiv e-prints* (2013)
174. Actis M, et al. *Experimental Astronomy* 32:193 (2011)
175. IceCube Collaboration, et al. *Astroparticle Physics* 26:155 (2006)
176. IceCube Collaboration. *Science* 342:1 (2013)
177. IceCube-Gen2 Collaboration, et al. *ArXiv e-prints* (2014)
178. Cahill-Rowley M, et al. *eprint arXiv* 1305:6921 (2013)
179. LaRosa TN, Kassim NE, Lazio TJW, Hyman SD. *AJ* 119:207 (2000)
180. Eisenhauer F, et al. *Astrophys. J.* 628:246 (2005)
181. Atoyan A, Dermer CD. *ApJ* 617:L123 (2004)
182. Quataert E, Loeb A. *Astrophys. J. Lett.* 635:L45 (2005)
183. Aharonian F, et al. *Astron. Astrophys.* 425:L13 (2004)
184. Kosack K, et al. *Astrophys. J. Lett.* 608:L97 (2004)
185. Albert J, et al. *Astrophys. J. Lett.* 638:L101 (2006)
186. Abdo AA, et al. *ApJS* 188:405 (2010)
187. Nolan PL, et al. *ApJS* 199:31 (2012)
188. Chernyakova M, et al. *ApJ* 726:60 (2011)
189. Profumo S. *Phys. Rev. D* 72:103521 (2005)
190. Belikov AV, Zaharijas G, Silk J. *Phys. Rev. D* 86:083516 (2012)
191. Cembranos JAR, Gammaldi V, Maroto AL. *JCAP* 4:51 (2013)
192. Acero F, et al. *Monthly Notices RAS* 402:1877 (2010)
193. Wang QD, Lu FJ, Gotthelf EV. *Mon. Not. R. Astron. Soc.* 367:937 (2006)
194. Hinton JA, Aharonian FA. *Astrophys. J.* 657:302 (2007)
195. Aharonian F, Neronov A. *Ap&SS* 300:255 (2005)
196. Aharonian F, Neronov A. *Astrophys. J.* 619:306 (2005)
197. Wang YP, Lu Y, Chen L. *Research in Astronomy and Astrophysics* 9:761 (2009)
198. Kusunose M, Takahara F. *ApJ* 748:34 (2012)
199. Guo YQ, Yuan Q, Liu C, Li AF. *Journal of Physics G Nuclear Physics* 40:065201 (2013)
200. Abramowski A, Gillessen S, Horns D, Zechlin HS. *MNRAS* 402:1342 (2010)
201. Aharonian F, et al. *Nature* 439:695 (2006)
202. Yusef-Zadeh F, et al. *ApJ* 762:33 (2013)
203. Macias O, Gordon C. *Phys. Rev. D* 89:063515 (2014)

204. Yoast-Hull TM, Gallagher III JS, Zweibel EG. *ApJ* 790:86 (2014)
205. Aharonian F, et al. *A&A* 503:817 (2009)
206. Ackermann M, et al. *ApJ* 750:3 (2012)
207. Daylan T, et al. *ArXiv e-prints* (2014)
208. Ackermann M, et al. *ApJ* 793:64 (2014)
209. Hooper D, Goodenough L. *Physics Letters B* 697:412 (2011), elsevier B.V.
210. Hooper D, Linden T. *Physical Review D* 84:123005 (2011)
211. Abazajian KN, Kaplinghat M. *Physical Review D* 86:83511 (2012)
212. Abazajian KN, Canac N, Horiuchi S, Kaplinghat M. *Phys. Rev. D* 90:023526 (2014)
213. Hooper D, Slatyer TR. *Physics of the Dark Universe* 2:118 (2013)
214. Hooper D. *Physics of the Dark Universe* 1:1 (2012)
215. Carlson E, Profumo S. *Phys. Rev. D* 90:023015 (2014)
216. Petrović J, Dario Serpico P, Zaharijaš G. *JCAP* 10:52 (2014)
217. Wang W, Jiang ZJ, Cheng KS. *MNRAS* 358:263 (2005)
218. Abazajian KN. *Journal of Cosmology and Astroparticle Physics* 03:010 (2011)
219. Hooper D, et al. *Phys. Rev. D* 88:083009 (2013)
220. Mirabal N. *MNRAS* 436:2461 (2013)
221. Calore F, Di Mauro M, Donato F. *ApJ* 796:14 (2014)
222. Cholis I, Hooper D, Linden T. *ArXiv e-prints* (2014)
223. Petrovic J, Serpico PD, Zaharijas G. *ArXiv e-prints* (2014)
224. Voss R, Gilfanov M. *A&A* 468:49 (2007)
225. Crocker RM. *ArXiv e-prints* (2014)
226. Weniger C. *Journal of Cosmology and Astroparticle Physics* 08:007 (2012)
227. Tempel E, Hektor A, Raidal M. *JCAP* 9:32 (2012)
228. Su M, Finkbeiner DP. *eprint arXiv* 1206:1616 (2012)
229. Ackermann M, et al. *Physical Review D* 88:82002 (2013)
230. Mertsch P, Sarkar S. *Physical Review Letters* 107:091101 (2011)
231. Crocker RM, Aharonian F. *Physical Review Letters* 106:101102 (2011)
232. Mou G, et al. *ApJ* 790:109 (2014)
233. Guo F, Mathews WG. *ApJ* 756:181 (2012)
234. Guo F, Mathews WG, Dobler G, Oh SP. *ApJ* 756:182 (2012)
235. Yang Rz, Aharonian F, Crocker R. *A&A* 567:A19 (2014)
236. Zubovas K, King AR, Nayakshin S. *MNRAS* 415:L21 (2011)
237. Fermi E. *Physical Review* 75:1169 (1949)
238. Axford WI, Leer E, Skadron G. *International Cosmic Ray Conference* 11:132 (1977)
239. Krymskii GF. *Akademiia Nauk SSSR Doklady* 234:1306 (1977)
240. Bell AR. *MNRAS* 182:147 (1978)
241. Blandford RD, Ostriker JP. *ApJ* 221:L29 (1978)
242. Webb GM, Drury LO, Biermann P. *A&A* 137:185 (1984)
243. Drury LO. *MNRAS* 251:340 (1991)
244. Malkov MA, Drury LO. *Reports on Progress in Physics* 64:429 (2001)
245. Strong AW, Moskalenko IV, Ptuskin VS. *Annual Review of Nuclear and Particle Science* 57:285 (2007)
246. Berezhinskii VS, Bulanov SV, Dogiel VA, Ptuskin VS (1990)
247. Moderski R, Sikora M, Coppi PS, Aharonian F. *Monthly Notices of the Royal Astronomical Society* 363 (2005)
248. Cox DP. *ARA&A* 43:337 (2005)
249. Schleicher DRG, Beck R. *A&A* 556:A142 (2013)